Available online at www.sciencedirect.com

ScienceDirect

Journal of Computational Physics 223 (2007) 865–897

JOURNAL OF COMPUTATIONAL PHYSICS

www.elsevier.com/locate/jcp

Interactions of breaking waves with a current over cut cells

Tingqiu Li *, Peter Troch, Julien De Rouck

Department of Civil Engineering, Ghent University, Technologiepark 904, B-9052 Zwijnaarde, Belgium

Received 4 November 2005; received in revised form 4 October 2006; accepted 5 October 2006
Available online 22 November 2006

Abstract

By design of the external and internal wave–current generators, the objective of this paper is to extend our efficient Navier–Stokes solver [T. Li, P. Troch, J. De Rouck, Wave overtopping over a sea dike, J. Comput. Phys. 198 (2004) 686–726] for modelling of interactions between breaking waves and a current over a cut-cell grid, based on a dynamic subgrid-scale (SGS) model. This solver is constructed by a novel VOF finite volume approach, coupled with surface tension. When studying waves following a positive current, our external generator creates the combined inflow motions of waves and a current, which is viewed as one type of wavy inflow conditions. For cases of waves against strong currents, our internal generator describes the opposing current, by incorporating the source function to the continuity and momentum equations as a net driving force, acting on the fluid elements lying within the finite thickness source region. The outgoing waves downstream are dissipated with a breaking-type wave absorber placed in the tank extremity. Five test cases recommended are of distinctly different applications of interest, characterized by overtopping of following waves over sloping and vertical structures.

Under the grid refinement effects, the results in 2D and 3D are in close agreement with the experimental data available in terms of the surface wave. Additionally, the performance of convergence in computations is also investigated, including full discussion for waves on beaches between 2D and 3D. By visualization of the motions that describe the physics of turbulence, it has been shown that our solver can capture most of the significant features in wave–current interactions varying with three different current speeds (positive, zero, negative).
© 2006 Elsevier Inc. All rights reserved.

Keywords: The Navier–Stokes solver; A numerical wave–current generator; Following or opposing waves; A breaking-type wave absorber

1. Introduction

Surface wave propagation in water of varying depth is of particular interest in the study of nonlinear wave-wave interactions and breaking wave-induced motions, especially coupling of steep waves with a structure. For the latter, the major physical processes involved are extremely complex, characterized by reflection, shoaling, diffraction and breaking, until waves overtop. Based on fluid mechanics of turbulence in waves, the dynamics of these transformations can be considered as small-scale turbulence, larger-scale coherent vortical

---

* Corresponding author. Tel.: +32 92645489; fax: +32 92645837.
E-mail address: tingqiu.li@UGent.be (T. Li).

0021-9991/$ - see front matter © 2006 Elsevier Inc. All rights reserved.
doi:10.1016/j.jcp.2006.10.003

motions, low-frequency waves and steady flows [2]. This subject itself, therefore, is one of the challenging topics in research and engineering. Importantly, the additional effects of a current substantially aggravate the situation that may change the coastal environments. Typically, the wave-induced currents alter the nearshore transport of sand and contaminants at the seabed, as the mechanism of sediment movement is closely related with pickup by wave action and transport by currents. Moreover, the combination of extreme wave and current conditions is also used to establish the design loads for large offshore structures.

The relevant study mainly involves computational modelling of moving boundary problems associated with an air–water interface (referred to as the free surface), separating the two segregated fluids. There are many ways available in theory for solution of this particular problem, which basically may be classified into two types of categories: one- and two-phase fluid model. In the case of the former, the free surface is assigned as one of boundaries, and a necessity is to specify boundary conditions at this surface before driving impulsively from rest; but conversely for the latter the free surface is viewed as a material interface of a contact discontinuity in variable density fields, captured naturally without special provision as part of the solution. Definitely, both methods are of their essential features. Given the exact location of interface at transient state, for example, a high order of accuracy is easily preserved with gravity-dominated one-phase solver [32], as in this case a non-smeared interface can be materialized. Additionally, computations are less expensive than a two-phase model, which needs the considerable CPU time, because of the extra air domain involved. Nevertheless, it indeed offers the potential to situations where an air bubble is trapped in the ambient water [25,38] and can well describe the behavior of the water–air mixture. Owing to the strong interface deformation and air entrainment phenomenon involved, the question raised here is relevant to numerical diffusion, primarily caused by handling a sharp jump of the density over a narrow band relying on the fact: the density and viscosity at a transitional layer between the two fluids vary appreciably across the interface. If such dissipation accumulates with time, this behavior could induce an impact on the accuracy and stability. Consequently, for high density ratio cases convergence may be slow, and the modelling of surface tension may lead to accuracy problems [36].

An earlier approach is based on the linear boundary layer approximation [20], when studying energy transfer between waves and a current. Until recently, the most popular one is to introduce the radiation stress concept [37], for instance, as the basis of the famous SWAN solver [4]. Within the framework of this technique, the wave motions are distinguished and are in fact separated from the current motions. An alternative is to account for surface-piercing numerical wavemakers for forcing surface waves. The emphasis is on modelling of external or internal wavemakers plus a current, by prescribing inflow conditions or adding a net driving force. This provides a convenient framework point for investigation of wave–current interactions in a consistent manner. More specifically, solution of the Navier–Stokes equations can directly give the current state and describe the wave pattern simultaneously. Importantly, distinction between waves and currents is unnecessary in this theory, as done in Park et al. [43]. It is one of the very few Navier–Stokes simulations even in the case of non-breaking waves. For situations where the positive (or negative) currents vary gradually in space and time, a key point in computations is that mass conservation has to be held over a long duration simulation, as waves develop rapidly in both scales. Accordingly, the numerical schemes proposed would identify the basic mechanical design feature. To avoid waves reflected in the near-inlet regions, one suggestion is to discretize a kind of Orlanski condition on a grid for the velocity and total wave profiles [30] or to apply for the internal wavemaker [35]. In view of the computational issues mentioned above, therefore, a numerical wavemaker has benefited greatly, especially it substantially differs from the radiation stress approaches.

In this paper, we mainly emphasize the design of an external and internal generator for wave–current coupling, by using a dynamic Smagorinsky model. Theoretically, an external generator can be viewed as one type of inflow conditions into the major computational domain [1,48], which perturbs flows through the boundary rather than the interior. It is a major difference with an internal generator, in which a net driving force is added to the source term of the governing equations for creation of the desirable adverse current. Both numerical generators provide an efficient tool for the study of coupling of breaking waves with a current over a sloping and vertical structure both in 2D and 3D, as addressed in waves following or opposing a current (mostly for the former). This considerably extends our previous study [30], in which only a pure wave in 2D is investigated with our developed Navier–Stokes solver, coupled to a static Smagorinsky model. The outgoing waves downstream are dissipated with the breaking-type wave absorber placed in the tank extremity.

Table 1
The wave and current characteristics for Case 1 to Case 5: the wave height H, the period T_a, the water depth d and a current speed U_c

Test cases	U_c (ms^{-1})	d (m)	H (m)	T_a (s)
Case 1 (WCA4): Kemp & Simons (UK)	−0.11, 0.0, 0.11	0.2	0.0394	1.0
Case 2: Klopman (Netherlands)	−0.16, 0.0, 0.16	0.5	0.12	1.44
Case 3 (WC1): Fredsøe et al. (Denmark)	−0.222, 0.0, 0.222	0.45	0.13	2.5
Case 4: a vertical wall problem	0.0, 0.10	0.7	0.16	2.0
Case 5: a seadike problem	0.0, 0.17	0.7	0.16	2.0

Five test cases without the exact solution are applied in this study, some of which are related to different applications in coastal and harbour engineering. Three cases first recommended involve the modelling of following (or opposing) waves with various wave characteristics (see Table 1) in the open channel flow over constant water depth, due to measurements available in the literature. In all test cases, particular interest is paid to the near-boundary free-surface turbulent region, especially when validated our design wave–current generators. The last two cases are characteristic of waves breaking in water of varying and constant depth, respectively, where steep waves overtop over the sea dike and vertical wall. Our results demonstrate that most of typical features in the wave-induced motions are captured with our solver in the presence of a current or not. Comparisons with the experimental data are also rather satisfactory in terms of the mean surface and horizontal velocity profiles, including prediction of the long-term propagation behavior of waves.

The outline of the present study is as follows. We first describe our numerical methods, e.g. by introducing a dynamic SGS model for the study of breaking water-wave problems, with particular emphasis on design of the wave–current generator plus the wave absorber. A comparison of the calculated results in 2D and 3D with the experimental data is represented next, followed by the concluding remarks.

2. Methodology

2.1. A MILES model

On the assumption that waves are travelling on a current in a numerical wave tank (NWT) that is of a relatively long flume (see Fig. 1), the plane of $z = 0$ corresponds to the mean water level in the Cartesian coordinate (x, y, z) system, where x is in the direction of the wave propagation, while (y, z) are toward the lateral direction and positive upwards, respectively. Based on MILES, the mathematical model in this study is governed by the unsteady incompressible Navier–Stokes (NS) equations, as the concept of MILES (monotonically integrated large-eddy simulation) attempts to resolve accurately the NS equations. Namely

$$\frac{\partial \varphi}{\partial t} + \frac{\partial (F_i - F_v + F_a)}{\partial x} + \frac{\partial (G_i - G_v + G_a)}{\partial y} + \frac{\partial (H_i - H_v + H_a)}{\partial z} = Q, \tag{1}$$

where the variables $\varphi = (0, u, v, w, \alpha)^T$, in which (u, v, w) are the components of the velocity in the x-, y- and z-directions, respectively, and α is the volume fractions in VOF (volume-of-fluid). By defining the inviscid fluxes (F_i, G_i, H_i), the viscous fluxes (F_v, G_v, H_v) and the other fluxes (F_a, G_a, H_a), we have

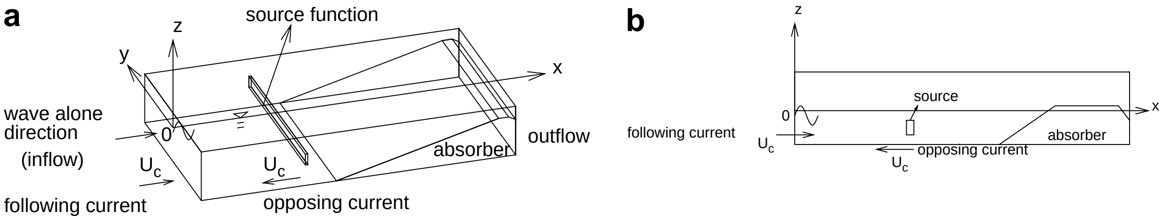

Fig. 1. Definition sketch of the NWT for waves following or opposing a current. (a) 3D; (b) 2D (on the symmetry plane, $y = 0$), where the origin is upstream.

$$F_{\rm i} = \begin{pmatrix} 0 \\ u^2 \\ vu \\ wu \\ 0 \end{pmatrix}, \quad G_{\rm i} = \begin{pmatrix} 0 \\ uv \\ v^2 \\ wv \\ 0 \end{pmatrix}, \quad H_{\rm i} = \begin{pmatrix} 0 \\ uw \\ vw \\ w^2 \\ 0 \end{pmatrix}, \tag{2}$$

$$F_{\rm v} = \begin{pmatrix} 0 \\ \tau_{xx} \\ \tau_{yx} \\ \tau_{zx} \\ 0 \end{pmatrix}, \quad G_{\rm v} = \begin{pmatrix} 0 \\ \tau_{xy} \\ \tau_{yy} \\ \tau_{zy} \\ 0 \end{pmatrix}, \quad H_{\rm v} = \begin{pmatrix} 0 \\ \tau_{xz} \\ \tau_{yz} \\ \tau_{zz} \\ 0 \end{pmatrix}, \tag{3}$$

$$F_{\rm a} = \begin{pmatrix} u \\ \frac{1}{\rho}p \\ 0 \\ 0 \\ u\alpha \end{pmatrix}, \quad G_{\rm a} = \begin{pmatrix} v \\ 0 \\ \frac{1}{\rho}p \\ 0 \\ v\alpha \end{pmatrix}, \quad H_{\rm a} = \begin{pmatrix} w \\ 0 \\ 0 \\ \frac{1}{\rho}p \\ w\alpha \end{pmatrix}, \tag{4}$$

plus the source terms Q

$$Q = \begin{pmatrix} f \\ \frac{1}{\rho}F_{\rm b}^x + F_{\rm d}^x + fu \\ \frac{1}{\rho}F_{\rm b}^y + F_{\rm d}^y + fv \\ \frac{1}{\rho}F_{\rm b}^z + F_{\rm d}^z + fw - g \\ \alpha\left(\frac{\partial u}{\partial x} + \frac{\partial v}{\partial y} + \frac{\partial w}{\partial z}\right) \end{pmatrix}, \tag{5}$$

where g is the gravitational acceleration and f is the internal source function (see Eq. (50)) for creation of an adverse current. $(F_{\rm b}^x, F_{\rm b}^y, F_{\rm b}^z)$ and $(F_{\rm d}^x, F_{\rm d}^y, F_{\rm d}^z)$ are three components of a body force $\vec{F}_{\rm b}$ [30] and an extra dissipative term $\vec{F}_{\rm d}$ (see Eq. (52)) in the (x, y, z)-directions, respectively. For the latter, it is active on a limited portion of regions (i.e. the so-called numerical damping zone, see Fig. 7) adjacent to the artificial boundary. For restricted domain simulations, this provides an alternative for dissipating energy of waves in numerical models. p is the modified pressure that considers the effect of the subgrid kinetic energy k (from the trace of τ_{ij}) by setting $p = P + \frac{2}{3}k$, in which P is the total pressure.

With the Einstein summation convention (such as $\tau_{xx} = \tau_{11}$), the viscous stress tensors τ_{ij} $(i,j = 1, 2, 3)$ may be evaluated by

$$\tau_{ij} = \nu\left(\frac{\partial u_i}{\partial x_j} + \frac{\partial u_j}{\partial x_i}\right) \tag{6}$$

with the molecular viscosity ν (a constant of $1.3 \times 10^{-4}\ \mathrm{m^2\ s^{-1}}$). The local density ρ and the viscosity ν are linearly connected with the scalar value α

$$\rho = \alpha\rho_{\rm w} + (1 - \alpha)\rho_{\rm a}, \quad \nu = \alpha\nu_{\rm w} + (1 - \alpha)\nu_{\rm a}, \tag{7}$$

where the subscripts (w, a) denote the water and air, respectively.

2.2. Solution procedures

Applying Gauss's divergence theorem to Eq. (1), this yields the integral form as

$$\frac{\partial}{\partial t}\int_V \varphi\, \mathrm{d}V + \int_S \mathbf{F} \cdot \mathrm{d}\mathbf{S} = \int_V Q\, \mathrm{d}V \tag{8}$$

for the surface S surrounding the domain of interest V. Accordingly, the discretization at the $(n+1)$th time level is driven by

$$\frac{\partial \varphi^{n+1}}{\partial t} = -\frac{1}{V}\sum_{\text{faces}} \widehat{\mathbf{F}}^{n+1} S + Q^{n+1} \tag{9}$$

over each cell of a hexahedron. $\sum$ represents the summation of all cell faces on a grid, and $\widehat{\mathbf{F}}$ includes the inviscid, viscous and other fluxes via

$$\widehat{\mathbf{F}} = \mathbf{F}\cdot\bar{n} = (F_\mathrm{i} - F_\mathrm{v} + F_\mathrm{a})n_x + (G_\mathrm{i} - G_\mathrm{v} + G_\mathrm{a})n_y + (H_\mathrm{i} - H_\mathrm{v} + H_\mathrm{a})n_z \tag{10}$$

with unit normal surface vector $\bar{n}$, where (n_x, n_y, n_z) are its three normal components outwards in the x-, y- and z-directions, respectively. $(F_\mathrm{i}, F_\mathrm{v}, F_\mathrm{a})$ to $(H_\mathrm{i}, H_\mathrm{v}, H_\mathrm{a})$ are the fluxes defined by Eqs. (2)–(4).

By introducing the delta form $\delta\varphi = \varphi^{n+1} - \varphi^n$ for the velocity, the fluxes $\widehat{\mathbf{F}}^{n+1}$ in Eq. (9) can be linearized locally with respect to time t, when dropping the high-order terms. Namely

$$\widehat{\mathbf{F}}^{n+1} = \widehat{\mathbf{F}}^n + \frac{\partial \widehat{\mathbf{F}}}{\partial \varphi}\delta\varphi \tag{11}$$

only for the convective and diffusion terms, resulting in Eq. (9) to be factored into the three one-dimensional equations as follows:

$$\begin{aligned} &-A_{i-1}\delta\varphi^{**}_{i-1} + A^{(1)}_p\delta\varphi^{**} - A_{i+1}\delta\varphi^{**}_{i+1} = \Delta t R,\\ &-A_{j-1}\delta\varphi^{*}_{j-1} + A^{(2)}_p\delta\varphi^{*} - A_{j+1}\delta\varphi^{*}_{j+1} = \delta\varphi^{**},\\ &-A_{k-1}\delta\varphi_{k-1} + A^{(3)}_p\delta\varphi - A_{k+1}\delta\varphi_{k+1} = \delta\varphi^{*}, \end{aligned} \tag{12}$$

based on the alternating direction implicit (ADI) approximate factorization with a local time step Δt. The subscripts $(i\pm 1, j\pm 1, k\pm 1)$ represent two adjacent neighbours of cell (i), respectively, and the coefficients $(A_{i\pm 1}, A_{j\pm 1}, A_{k\pm 1})$ typically involve a blend of the inviscid and viscous volumetric fluxes. R in Eq. (12) is the residual of the momentum equations defined as

$$R = -\left\{\frac{1}{V}\sum_{\text{faces}}\left(\overline{F}^n_\mathrm{i} - \overline{F}^n_\mathrm{v}\right) - Q^n\right\} \tag{13}$$

with $\overline{F}_\mathrm{i} = F_\mathrm{i}n_x + G_\mathrm{i}n_y + H_\mathrm{i}n_z$ and $\overline{F}_\mathrm{v} = F_\mathrm{v}n_x + G_\mathrm{v}n_y + H_\mathrm{v}n_z$, where the source terms $Q^{n+1} = Q^n = (0,0,0,-g)^\mathrm{T}$, indicating that the body force $\vec{F}_\mathrm{b}$, the dissipative term $\vec{F}_\mathrm{d}$, the source function $f(x,y,z,t)$ and the other fluxes are retained in the explicit formulation during the implicit process.

When the contribution of the dissipative component F^x_d and the source function f is incorporated into the temporal velocity ũ (for example, for the momentum equations in the x-direction)

$$\tilde{u} = u^n + \delta u + \Delta t\left(\frac{1}{\rho}F^x_\mathrm{b} + F^x_\mathrm{d} + fu\right) \tag{14}$$

this results in the Poisson equation for the pressure as

$$\nabla\cdot\frac{\nabla p^{n+1}}{\rho^{n+1}} = \frac{1}{\Delta t}\{\nabla\cdot\vec{\tilde{u}} - f\} \tag{15}$$

according to the projection algorithm. In our implicit stage, the convective fluxes $\overline{F}^n_\mathrm{i}$ (see Eq. (13)) at the nth time step are calculated by means of the flux-difference splitting approach, yielding the fluxes $\overline{F}^n_\mathrm{i}$ at the face $(i+\frac{1}{2})$ between cell (i) and its neighbour $(i+1)$

$$\left(\overline{F}^n_i\right)_{i+\frac{1}{2}} = \left(u_n S u^\mathrm{L}\right)_{i+\frac{1}{2}} \quad \text{when } (u_n)_{i+\frac{1}{2}} > 0. \tag{16}$$

Under the finite volume approximation, two typical variables (u_n, u^L) are separately treated for maintaining the second-order spatial accuracy, including enhancement of the numerical stability. First, the normal face velocity u_n (defined by $u_n = un_x + vn_y + wn_z$) is directly modified by our design combination of the second- and fourth-order artificial damping terms. Namely

$$(u_n)_{i+\frac{1}{2}} = \frac{1}{2}\left\{(u_n)_i + (u_n)_{i+1}\right\} - \left\{\frac{1}{2\rho\psi_2 c_2}\left(p^{\mathrm{R}}_{i+\frac{1}{2}} - p^{\mathrm{L}}_{i+\frac{1}{2}}\right)_1 - \frac{1}{2\rho\psi_4 c_4}\left(p^{\mathrm{R}}_{i+\frac{1}{2}} - p^{\mathrm{L}}_{i+\frac{1}{2}}\right)_3\right\}. \tag{17}$$

As expected, this correction helps to damp high frequency oscillations, since for problems of the convective domination the linear interpolation of the face value results in an unbounded solution. Secondly, the relevant face values (such as the left state u^{L}) are estimated with the characteristic variables at adjacent cells, by incorporating the second-order essentially non-oscillatory (ENO) scheme for $u^{\mathrm{L}}_{i+\frac{1}{2}}$ and $\alpha_i + \frac{1}{2}^{\mathrm{L}}$, and the MUSCL (monotone upstream-centered scheme for conservation laws) approach for $(p_i + \frac{1}{2}^{\mathrm{R}})_3$ and $(p_i + \frac{1}{2}^{\mathrm{L}})_3$, while an one-order upwind discretization is used for $(p_i + \frac{1}{2}^{\mathrm{R}})_1$ and $(p_i + \frac{1}{2}^{\mathrm{L}})_1$. Finally, Eq. (16) in the ENO context is derived by

$$(\overline{F}^n_i)_{i+\frac{1}{2}} = \begin{cases} u_n S[\frac{1}{2}(u_i + u_{i+1}) - \frac{1}{8}\frac{\partial^2 u}{\partial x^2}\Delta x^2] & \text{if } |u_i + 1 - u_i| \leqslant u_i - u_{i-1}|, \\ u_n S[\frac{1}{2}(3u_i - u_{i-1}) + \frac{3}{8}\frac{\partial^2 u}{\partial x^2}\Delta x^2] & \text{otherwise,} \end{cases} \tag{18}$$

in smooth regions. Based on Taylor series, the different leading-order truncation errors ($\frac{1}{8}\frac{\partial^2 u}{\partial x^2}\Delta x^2$, $\frac{3}{8}\frac{\partial^2 u}{\partial x^2}\Delta x^2$) are obtained, dependent on the upwinding of the stencils. For Eq. (17), our damping terms with regard to the pressure can be expressed by

$$-\left\{\frac{1}{2\rho\psi_2 c_2}(p_{i+1} - p_i) - \frac{1}{12\rho\psi_4 c_4}(-p_{i+2} + 3p_{i+1} - 3p_i + p_{i-1})\right\}, \tag{19}$$

where the scaling factor c_4 ($c_2 = 1$ in this case) is determined by the three mainly diagonal coefficients ($A^{(1)}_p, A^{(2)}_p, A^{(3)}_p$) of Eq. (12), which is formulated according to [30], in case the second- and fourth-order coefficients (ψ_2, ψ_4) are given adaptively with the local diffusion velocity. Both schemes can be considered as one type of shock-capturing schemes [16], which provide a particular form of the functional reconstruction for the convective fluxes: by using TVD (total variation diminishing)-based schemes as flux limiters that are implicitly implemented SGS models. Definitely, such features essentially construct one type of MILES for the spatial discretization of the convective terms. Hopefully, the scheme rendered prevents unphysical oscillations in computations.

More importantly, a hybrid approach constructed by the weighted upwind scheme and blending algorithm is devised for high resolution of a step profile of α in VOF, as opposed to geometrical strategies. It is a simple but effective algorithm in multidimensional directions, characterized by the interfaces that are arbitrarily orientated with respect to the computational grids. To achieve higher-order accuracy, for example, the volume fractions $\alpha_i + \frac{1}{2}^n$ in VOF are updated by adding the second-order correction that accounts for the flux limiting

$$\alpha^n_{i+\frac{1}{2}} = \Gamma\alpha^n_i + (1 - \Gamma)(-\alpha^{\mathrm{L}}_{i+\frac{1}{2}}) \quad \text{if } \alpha^n_{i-1} \text{ or } \alpha^n_{i+1} \neq 0 \tag{20}$$

implying that a bounded solution can be guaranteed during tracking. In particular, the high-resolution monotone scheme for $\alpha_i + \frac{1}{2}^{\mathrm{L}}$ may adjust amount of the numerical diffusion induced by the low-order scheme (this feature is also suitable to Eq. (17), as done in the flux-corrected transport algorithms, by introduction of a flux-limiter Γ. For the fully implicit cell-staggered finite volume (FV) method on non-uniform stationary cut-cell grids, we refer the reader to our study [30,33] for considerable detail of this procedure. The following is to describe a dynamic subgrid-scale (SGS) model, because MILES coupled to such model can give a better accuracy for particular periodic breaking water-wave propagation problems, as guided by the results of Appendix A (e.g. Figs. 25 and 26).

2.3. A dynamic Smagorinsky's model

In the conventional LES (large-eddy simulation), the SGS stress β_{ij} caused by nonlinear terms $\overline{u_i u_j}$ is expressed as

$$\beta_{ij} = \overline{u_i u_j} - \overline{u}_i \overline{u}_j \tag{21}$$

in case a low-pass filter is applied to the NS equations. The overbar represents the spatially filtered quantities at a characteristic length scale of the small eddies $\overline{\Delta}$, based on the predefined filter kernel (e.g. a top-hat shaped kernel). In the present study, we address the issue of modeling the total stress term (i.e. a purely dissipative term). On the assumption that the SGS stress is restricted to eddy-viscosity branch of a family, theoretically, it may be cast into the constitutive relation as follows:

$$\beta_{ij} - \frac{1}{3}\delta_{ij}\beta_{kk} = -2\nu_{\mathrm{T}}\overline{S}_{ij} \quad \text{with } \overline{S}_{ij} = \frac{1}{2}\left(\frac{\partial \overline{u}_i}{\partial x_j} + \frac{\partial \overline{u}_j}{\partial x_i}\right), \tag{22}$$

where δ_{ij} and $\overline{S}_{ij}$ are the Kronecker delta function and the resolved-scale strain rate tensor, respectively. Physically, the major role of the SGS model is to remove energy from the resolved scales. In this sense, Eq. (6) can be rewritten as

$$\tau_{ij} = \nu_{\mathrm{eff}}\left(\frac{\partial \overline{u}_i}{\partial x_j} + \frac{\partial \overline{u}_j}{\partial x_i}\right) \tag{23}$$

as the isotropic part of the SGS stresses ($\frac{1}{3}\delta_{ij}\beta_{kk}$) has been absorbed to the pressure term. An essential point in our MILES, now, is to evaluate the effective viscous coefficient ν_{eff}, assigned with $\nu_{\mathrm{eff}} = \nu + \nu_{\mathrm{T}}$, by introducing a dynamic Smagorinsky's model (DSM) that captures the averaged motions without elaborate numerical computation.

Owing to the simplicity, a Smagorinsky-type isotropic eddy-viscosity model remains in wide use [28], as small scales tend to be more isotropic than the large-scale fluctuations, which are simulated directly. Theoretically, the DSM model eliminates the uncertainty in a static Smagorinsky model (SSM) [50], especially helps to correlate with varying in different regions of the flow (see Fig. 17 for the eddy viscosity contours). An attractive benefit is to avoid the free-surface boundary conditions specified, as the satisfactory conditions is usually lack for the turbulent variables involved, for example, by using a k–ϵ turbulence model. Consequently, a simple DSM is coupled to our shock-capturing scheme as the blending algorithm: MILES + SGS. Hopefully, it becomes a promising LES approach for modelling of breaking water-wave propagation problems. One way is capable of capturing the inherently anisotropic small-scale flow features, as in MILES implicit SGS models provide an additional damping, caused by nonlinear high-frequency filters built-in the convection discretization.

Within the framework of the eddy-viscosity technique, the introduction of the DSM is adaptively to estimate the adjustable dimensionless parameter C_{s}, related with the unknown eddy viscosity ν_{T}. Namely

$$\nu_{\mathrm{T}} = C_{\mathrm{s}}(\overline{\Delta})^2|\overline{S}|, \tag{24}$$

where $|\overline{S}|$ is the Frobenius norm of the strain tensor rate $\overline{S}_{ij}$, setting by $|\overline{S}| = \sqrt{2\overline{S}_{ij}\overline{S}_{ij}}$. In this case, it is evaluated with the magnitude of the vorticity vector by definition of $|\overline{S}| = |\nabla \times \vec{\overline{V}}|$, where $\nabla = \left(\frac{\partial}{\partial x}, \frac{\partial}{\partial y}, \frac{\partial}{\partial z}\right)$ and $\vec{\overline{V}} = \overline{u}\vec{i} + \overline{v}\vec{j} + \overline{w}\vec{k}$. Additionally, the constraint $C_{\mathrm{s}} = \max(C_{\mathrm{s}}, 0)$ is artificially enforced whenever C_{s} returns negative values, implying that no mechanism for backscatter is allowed, as done in Smagorinsky's constant model [30]. It is absolutely dissipative in computations, probably guaranteeing numerical stability.

Based on the multiple filtering operators [17], the subtest-scale stress tensor similar to Eq. (21) also holds by

$$T_{ij} = \widetilde{\overline{u_i u_j}} - \tilde{\overline{u}}_i\tilde{\overline{u}}_j \tag{25}$$

provided that the test filter $\tilde{\overline{\Delta}}$ (denoted by a tilde) is introduced and used in fact as the second filter to the NS equations. For situations involving the same shape in the filter kernel as the grid filter $\overline{\Delta}$, the filter width of $\tilde{\overline{\Delta}}$ is typically a function of $\overline{\Delta}$. Owing to the scale-similarity in the algebraic identity, the resolved turbulent stresses D_{ij} are obtained by

$$D_{ij} = T_{ij} - \tilde{\beta}_{ij}(\widetilde{\overline{u_i u_j}} - \tilde{\overline{u}}_i\tilde{\overline{u}}_j) - (\widetilde{\overline{u_i u_j}} - \widetilde{\overline{u}_i\overline{u}_j}) = \widetilde{\overline{u}_i\overline{u}_j} - \tilde{\overline{u}}_i\tilde{\overline{u}}_j, \tag{26}$$

which removes the problem in estimate of the quantity $\widetilde{\overline{u_i u_j}}$. Under a refined discrete filter given (see Eq. (34), D_{ij} can be exactly evaluated with the resolved scales, as it physically represents the contribution of the smallest resolved length scales to the Reynolds stresses.

On the other hand, the anisotropic subgrid-scale stresses β_{ij} and subtest-scale ones T_{ij} are formulated by, respectively,

$$
\begin{aligned}
\beta_{ij} - \frac{1}{3}\delta_{ij}\beta_{kk} &= -2\nu_t\bar{S}_{ij} = -2C_s\left(\bar{\Delta}\right)^2|\bar{S}|\bar{S}_{ij},\\
T_{ij} - \frac{1}{3}\delta_{ij}T_{kk} &= -2\widetilde{\nu_t\bar{S}_{ij}} = -2C_s\left(\tilde{\bar{\Delta}}\right)^2|\tilde{\bar{S}}|\tilde{\bar{S}}_{ij}.
\end{aligned}
\tag{27}
$$

Substituting Eq. (27) into Eq. (26), this yields

$$
D_{ij} = -2C_s(\bar{\Delta})^2\left\{(\tilde{\bar{\Delta}}/\bar{\Delta})^2|\tilde{\bar{S}}|\tilde{\bar{S}}_{ij} - \widetilde{|\bar{S}|\bar{S}_{ij}}\right\}. \tag{28}
$$

To achieve more stable values of C_s, Eq. (28) is replaced with a least-square manner that accounts for the effects of all the components [29]. This ensures the error E to be minimal

$$
E = (D_{ij} + 2C_s(\bar{\Delta})^2 P_{ij})^2 \tag{29}
$$

by forcing $\frac{\partial E}{\partial(C_s(\bar{\Delta})^2)} = 0$. Thus, we have

$$
C_s(\bar{\Delta})^2 = -\frac{\langle D_{ij}P_{ij}\rangle^*}{2\langle P_{ij}P_{ij}\rangle^*} \tag{30}
$$

with P_{ij} defined by

$$
P_{ij} = (\tilde{\bar{\Delta}}/\bar{\Delta})^2|\tilde{\bar{S}}|\tilde{\bar{S}}_{ij} - \widetilde{|\bar{S}|\bar{S}_{ij}}, \tag{31}
$$

where the variation of C_s on the scale of the test filter width $\tilde{\bar{\Delta}}$ is ignored. Because of the filter-grid ratio $\gamma = \bar{\Delta}/\bar{\Delta} = 2$ (usually and more smooth than $\gamma = 4$, as shown in Fig. 2), the estimate of P_{ij} is not necessary to define the values $\tilde{\bar{\Delta}}$ and $\bar{\Delta}$, respectively. This feature is useful in some cases, as the flow structure near a wall seems very anisotropic, leading to the definition of the length scale for anisotropic grids or filters unclear [11].

The sign $\langle\ \rangle^*$ stands for the averaging operation over the homogeneous directions, which is introduced additionally, for example, by using the following trapezoidal filter:

$$
\begin{aligned}
\langle\phi\psi\rangle_{i,j,k} = {} & \frac{9}{16}(\phi\psi)_{i,j,k} + \frac{3}{32}\{(\phi\psi)_{i+1,j,k} + (\phi\psi)_{i,j,k+1} + (\phi\psi)_{i-1,j,k} + (\phi\psi)_{i,j,k-1}\}\\
& + \frac{1}{64}\{(\phi\psi)_{i+1,j,k+1} + (\phi\psi)_{i-1,j,k+1} + (\phi\psi)_{i-1,j,k-1} + (\phi\psi)_{i+1,j,k-1}\}.
\end{aligned}
\tag{32}
$$

Eq. (32) implies that averaging in the wall-normal direction (i.e. along the y-axis) is performed over eight neighboring grid points surrounding its center (i,j,k), which avoids very small denominators or negative numerator values. One problem is in the near-wall regions, where turbulent flows are characterized by much less universal properties. Owing to some mathematical inconsistencies with the formulation of filtering operation, it appears that Eq. (30) is not applicable to general geometries, as C_s is actually a function of time and position [18]. For the present water-wave propagation problems involved, however, we focus attention on the

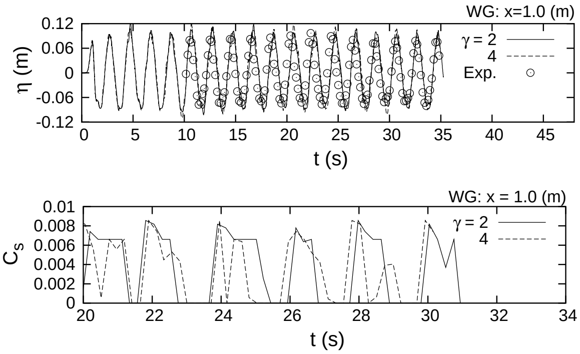

Fig. 2. Computations with two different filter-grid ratios γ over grids (251 × 40) for Case 5 (pure regular waves): the time evolution of the surface elevation η and Smagorinsky's parameter C_s (on the free surface) with $\gamma = 2$ and 4.

capture of high turbulence that dominates over the wave-induced motions, generated in waves breaking. In this sense, such problem associated with the breaking waves may be thought of as a kind of isotropic decaying turbulence, due to without the fluctuation of walls (if assuming that far from walls the SGS flow is ideally considered homogeneous isotropic). For this reason, the dynamic model can remove the mathematical inconsistencies, i.e. C_s can depend only on time (see Fig. 2) during averaging, as conducted with Eq. (32). With possibilities of simultaneously handling flow and grid anisotropies, on the other hand, our MILES may give a better approach for inhomogeneous turbulent flows near the free-surface (or solid walls), because of the anisotropic features of the SGS modeling in MILES [15].

To ensure smooth C_s, three times in cycle seem enough, based on our experience. When evaluating P_{ij} (see Eq. (31) with inclusion of the vorticity components, a favourable choice is with high-order numerical methods, for example, by using a fourth-order central-difference approximation in smooth regions. In this way, the first-order derivative, $(\frac{\partial \overline{u}}{\partial x})_i$ in the ith direction (where $\overline{u}_i$ denotes a variable on the grid, and Δx is the grid size in the relevant direction) is given by

$$\left(\frac{\partial \overline{u}}{\partial x}\right)_i = \frac{-\overline{u}_{i+2} + 8\overline{u}_{i+1} - 8\overline{u}_{i-1} + \overline{u}_{i-2}}{12\Delta x}, \tag{33}$$

while a central-difference scheme is employed in the near-wall regions and adjacent to the free surface. To remove the high spatial frequencies, moreover, we utilize a seven-point discrete test filter with trapezoidal rule integration [51] for estimate of a filtered variable on the grid $\widetilde{\overline{u}}$ (see Eq. (26), i.e.

$$(\widetilde{\overline{u}})_i = \frac{1}{64}\{\overline{u}_{i-3} - 6(\overline{u}_{i-2} + \overline{u}_{i+2}) + 15(\overline{u}_{i-1} + \overline{u}_{i+1}) + \overline{u}_{i+3} + 44\overline{u}_i\} \tag{34}$$

in smooth regions but weights for symmetric filter with three- or five-point vanishing moments elsewhere. The filtering is performed over regions of a sequence of one-dimensional filter for 2D or 3D problems. It can eliminate the highest wavenumber that could be sustained by the grid [40], as the function becomes zero at the grid cutoff in spectral space, despite the absence of the inconsistency in the effective filter width for Eq. (34). Note that we do not introduce a weighting function that accounts for the non-uniform grid spacing effects, as done in our ship flow studies for filtering the wave height over a stretched grid [32].

Based on the DSM, a smooth function of C_s varying with time is given, as illustrated in Fig. 2, where the shape of C_s forms a more regular step function, when $\gamma = 2$. By comparison, the DSM produces the better and less physical dissipation behavior for the free-surface profiles, as in our study Smagorinsky's coefficient is constant ($C_s = 0.01$), according to the SSM. Interestingly, the computations are not much sensitive to the filter-grid ratio γ (although $\gamma = 2$ looks better), especially a large variation on C_s does not have too much of a bearing on the results. One reason for that is there exists no net effect of the SGS model due to $\nu_T = 0$, in case the derivative of the velocity $(\frac{\partial u}{\partial z})$ is small, where C_s may be huge. The relevant studies in the literature are given with [39,45,52], including two new SGS models, a dynamic free-surface function model (DFFM) and a dynamic anisotropic selective model (DASM), proposed by Shen and Yue [49].

2.4. Initial and boundary conditions

2.4.1. Initial conditions

At $t = 0$, all simulations start from a state of rest in quiescent water via $(u, v, w) = 0$ plus the hydrostatic pressure distribution in the entire computational domain. After that, the accelerator in fluid fixed at the inflow boundary will vertically oscillate the static water, and as a result of forcing surface waves propagating towards the positive x-direction.

According to a flat free-surface at $t = 0$, the volume fractions α in VOF are initially assigned by

$$\alpha = \begin{cases} 1 & \text{in the full fluid,} \\ \frac{\eta + d - z_{k-1}}{\Delta z_k} & \text{over mixed cell,} \\ 0 & \text{in the air,} \end{cases} \tag{35}$$

where η is the surface elevation (setup and setdown) with respect to the still water line, Δz is the vertical grid size and the index k represents the mixed cell pointing to the free surface.

2.4.2. Boundary conditions

On the assumption that the free surface only supports the normal stress of a constant surface tension, the more accurate normal free-surface boundary condition for the pressure (despite the absence of wind) is expressed by

$$p = \rho v_{\mathrm{eff}} \left\{ 2\frac{\partial w}{\partial z} - \frac{\partial \eta}{\partial x}\left(\frac{\partial u}{\partial z} + \frac{\partial w}{\partial x}\right) - \frac{\partial \eta}{\partial y}\left(\frac{\partial v}{\partial z} + \frac{\partial w}{\partial y}\right) \right\} \tag{36}$$

as in our solver surface tension has been handled with a body force. Of course, Eq. (36) has been used for the study of turbulent free-surface flows in 3D modern ships [32], which is referred to as the Reynolds stress free-surface boundary condition. It essentially represents the normal force only acting on the free surface under the pressure surrounding air. A major benefit is that such boundary condition offers the potential for the capture of the (thin) free-surface wave boundary layer, especially in waves breaking.

At the seabed, the free slip conditions are enforced and the no-flux condition is used on a cut cell (defined by a cell partially dry) that is utilized for handling an arbitrary geometry, while the no-slip conditions are implemented in the lateral direction. Additionally, a kind of Orlanski linear open boundary condition is employed at the outflow boundary

$$\frac{\partial \varphi}{\partial t} + (C + U_{\mathrm{c}})\frac{\partial \varphi}{\partial x} = 0, \tag{37}$$

where $\varphi = (u, v, w, \alpha, p)$. C is the phase velocity of the long wave and its upper limit value is set by $C = \sqrt{gd}$ in water of finite depth d. Theoretically, Eq. (37) simulates the propagation of velocity waves out of the computational domain. Unfortunately, the energy of waves is reflected there (see Fig. 9), implying that the use of such condition is not expected with high absorption efficiency (probably, due to approximation of the phase velocity). By comparison, an alternative is to introduce the physical wave absorber device for a tank, which would be given, following the explanation of our design wave–current generator as inflow conditions.

2.5. An external wave–current generator

By superimposing a steady current onto waves, the combined motions on the inflow boundary are easily obtained with the linear wave theory, which turns out to give a substantial solution (i.e. inflow conditions) in regions of irrotational flow, as the nonlinear features of the free surface can be captured in the interior of the fluid. In the context of this theory, the reflected wave elevation η_{f} at the inlet can be estimated with the incident wave elevation η_{i} specified via

$$\eta_{\mathrm{f}} = \eta_{\mathrm{t}} - \eta_{\mathrm{i}} \tag{38}$$

provided that the total wave elevation η_{t} is generated. The subscripts $(\mathrm{t}, \mathrm{f}, \mathrm{i})$ represent the total, reflected and incident waves, respectively. Since we concern the steady vertically-uniform current speed U_{c} [44], the reflected waves η_{f} can be satisfied the modified Orlanski's theory [42]. This yields

$$\frac{\partial \eta_{\mathrm{f}}}{\partial t} - (C_x + U_{\mathrm{c}})\frac{\partial \eta_{\mathrm{f}}}{\partial x} = 0. \tag{39}$$

Substituting Eq. (38) into Eq. (39), the resulting wave surface is given by

$$\frac{\partial \eta_{\mathrm{t}}}{\partial t} - (C_x + U_{\mathrm{c}})\frac{\partial \eta_{\mathrm{t}}}{\partial x} = \frac{\partial \eta_{\mathrm{i}}}{\partial t} - (C_x + U_{\mathrm{c}})\frac{\partial \eta_{\mathrm{i}}}{\partial x} \tag{40}$$

indicating that the net waves relative to the weak disturbance of the reflected waves are created at the inflow boundary. Substantially, the final result can be considered as the addition of driving force similar to the contribution under the gravity acceleration. Mathematically, it is constructed as the 1D hyperbolic wave equation for the total wave η_{t}. C_x in Eq. (40) is the component of the group celerity in the x direction, and for any wave propagation its derivation is always as follows:

$$C_x = \frac{\partial \omega_r}{\partial k} = \frac{1}{2k}\left\{1 + \frac{2kd}{\sinh(2kd)}\right\}\omega_r, \tag{41}$$

subject to the intrinsic angular frequency ω_r (the zeroth order approximation) and the wavenumber k defined by

$$\omega_r^2 = gk\tanh\{kd\} \quad \text{and} \quad k = \frac{2\pi}{\lambda}, \tag{42}$$

where the wavelength λ is precomputed from Eq. (49) below.

When solving this type of initial value problems, applying the second-order explicit Adams–Bashforth formulation yields

$$\eta_{\mathrm{t}}^{n+1} = \eta_{\mathrm{t}}^{n} + \Delta t R^n + \frac{\Delta t}{2}(R^n - R^{n-1}) \tag{43}$$

with an adaptive time step Δt, that accounts for the variation of the subgrid spacing plus the flow in the interior of domain, and the residual R defined by

$$R = \frac{\partial \eta_{\mathrm{i}}}{\partial t} - (C_x + U_{\mathrm{c}})\frac{\partial(\eta_{\mathrm{i}} - \eta_{\mathrm{t}})}{\partial x}, \tag{44}$$

where the desirable incident waves are specified a priori at the location of the inflow boundary.

According to our previous study [30], the use of Eq. (40) helps to guarantee a consistent manner in solving α due to a well-suited boundary value at the mixed cell even in the presence of a current. In particular, it only creates the very weak reflected waves.

Based on the velocity potential in fluid, the wave elevation η_{i} at ghost cells is given by

$$\eta_{\mathrm{i}} = \sum_{j=1}^{m}\left\{\frac{H}{2}\cos\left[k\left(x + \frac{\lambda}{4}\right) - \omega_{\mathrm{a}} t\right]\right\}_j \tag{45}$$

along a vertical wavemaking boundary in 2D. With the help of Eq. (44), the principal source term eventually becomes

$$\frac{\partial \eta_{\mathrm{i}}}{\partial t} - (C_x + U_{\mathrm{c}})\frac{\partial \eta_{\mathrm{i}}}{\partial x} = \sum_{j=1}^{m}\left\{\frac{H_j}{2}[\omega_{\mathrm{a}} + (C_x + U_{\mathrm{c}})k]_j \sin\left[k\left(x + \frac{\lambda}{4}\right) - \omega_{\mathrm{a}} t\right]_j\right\} \tag{46}$$

for the combined motions of irregular waves and a current, as it evolves in time t (where the variable (x) is fixed). m denotes the total number of waves (obviously, the simplest is $m = 1$ for a target of regular waves), and the subscript j means the jth component. Given the standard wave energy spectrum of irregular wave trains, the desirable irregular waves can be created by linearly superimposing a series of regular waves to a specified number of terms ($m = 10$, enough for our computations), as illustrated in Fig. 3, when the characteristics of one basic single regular wave (the wave height H and period T_{a}) is specified.

Owing to a Doppler shifted frequency ($kU_{\mathrm{c}}\cos\beta$), the absolute frequency ω_{a} can be evaluated by

$$\omega_{\mathrm{a}} = \omega_r + kU_{\mathrm{c}}\cos\beta \quad \text{or} \quad \omega_{\mathrm{a}} = \frac{2\pi}{T_{\mathrm{a}}}, \tag{47}$$

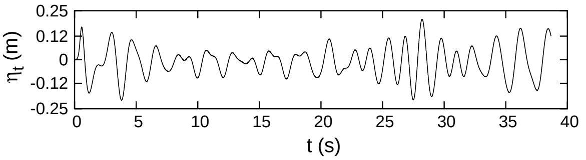

Fig. 3. Generation of irregular waves at the inlet, based on the significant wave height ($H = 0.16$ m) and the wave peak period ($T_{\mathrm{a}} = 2.0$ s) in the presence of a current ($U_{\mathrm{c}} = 0.14\ \mathrm{ms}^{-1}$).

where β is an angle of the wave orthogonal with the current streamline. In our present study, it is set to zero, as waves propagate into a current without obliqueness.

Given the knowledge of the discrete quantity for η_t (see Fig. 3), it is easy to obtain the corresponding velocity distributions at the inflow boundary. One way is that three components (u_t, v_t, w_t) of the velocity for the total waves can be represented by superposing linearly the steady current speed U_c onto the velocity induced by incident waves that absorb the Doppler shifted frequency. This yields

$$\begin{aligned} u_t &= U_c\cos\beta + \sum_{j=1}^{m}\left\{\frac{H}{2}(\omega_a - kU_c\cos\beta)\frac{\cosh\{k(\eta_t+d)\}}{\sinh(kd)}\cos\left[k\left(x+\frac{\lambda}{4}\right)-\omega_a t\right]\right\}_j, \\ v_t &= 0, \\ w_t &= \sum_{j=1}^{m}\left\{\frac{H}{2}(\omega_a - kU_c\cos\beta)\frac{\sinh\{k(\eta_t+d)\}}{\sinh(kd)}\sin\left[k\left(x+\frac{\lambda}{4}\right)-\omega_a t\right]\right\}_j. \end{aligned} \tag{48}$$

Accordingly, the wavelength λ that absorbs a current is derived by

$$\lambda = \left\{\left[\frac{g\lambda}{2\pi}\tanh\frac{2\pi d}{\lambda}\right]^{\frac{1}{2}} + U_c\cos\beta\right\}T_a, \tag{49}$$

which is solved iteratively, based on Newton–Raphson's technique that can give rapid convergence, under the period T_a and depth d specified. As a consequence, Eqs. (40) and (48) construct the basis of our external generator as wavy inflow boundary conditions for the wave–current coupling. The major mechanism is that the effects of the steady current have been absorbed to the wavelength (see Eq. (49), related with the Doppler-shifted linear dispersion relation) together with the velocity profiles (see Eq. (48), corresponding to full potential theory), while the combined flows are realized by superimposing a current onto waves.

We first apply our external generator for modelling of waves travelling on three different current speeds (positive, zero, negative), which can be recognized in Fig. 4 (refer to Fig. 5 for its geometry). By observation, the external generator did well in the case of waves following a positive current, as the positive net flux formed by the boundary can maintain the energy balance in the NWT over a long duration simulation. But it fails to work for waves opposing the adverse current, in case the current is assigned as a net mass transport. Some reasons may be interpreted as the fact: the fluid leaving through the inflow boundary could drain water out of the tank, leading to a continuous drop in the mean water level. To solve particular counter current problems, the water has to be fed into the flow domain by the outflow boundary, as done in our study [34]. In this way, the computational domain is usually coupled with a numerical damping zone, which costs the substantial CPU time plus the heavy memory, resulting in convergence to be extremely slow in general. Hence, a hopeful alternative is to apply our internal generator, as described below, which creates an adverse current (see Figs. 14–16), based on the source function. A major feature is that our NWT can be made as much small as possible (at least in length), because of the use of a breaking-type wave absorber. This further maintains the minimal expense for computations without instability problem even for lengthy computations.

Fig. 5 demonstrates a typical example regarding wave-structure coupling problems with and without a positive current, by using the external generator. When the synthetic inflow motions fully develop and propagate along the tank, the following waves overtop over a vertical barrier in the front of a pier, and then the waves are strongly reflected at the seawall, as one case of the diffraction of regular and irregular waves by a barrier sitting

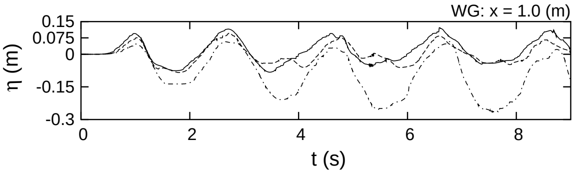

Fig. 4. Computations with three different currents (positive, zero, negative) over grids (251 × 40) for Case 4 (regular waves): the wave train at a certain position, by using the external generator. —— $U_c = 0.1\ \mathrm{ms}^{-1}$; – – – $U_c = 0.0$; – · – $U_c = -0.1\ \mathrm{ms}^{-1}$.

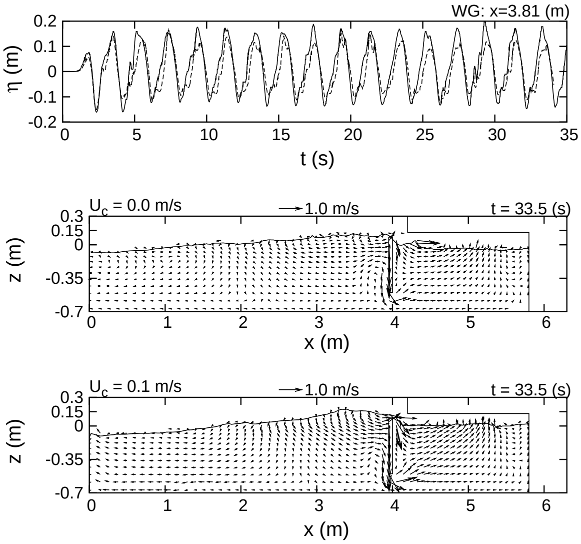

Fig. 5. Following-current-wave effects over grids (251 × 40) for Case 4 (regular waves): the wave train at a certain location and the instantaneous velocity fields. —— $U_c = 0.1\ \text{ms}^{-1}$; – – – $U_c = 0.0$.

above the bottom (see [31] for its 3D computations). From observation on this figure, the presence of the current causes substantial changes for the water-wave dynamics, especially in the near-barrier region, characterized by a horizontal large-scale eddy shed from the barrier (also see Fig. 26 for the irregular waves). Closed to the barrier, a violent overtopping jet occurs and surface waves naturally break against this structure, leading to high turbulence induced by the breaking waves, and as a result of increase of the wave-induced loading acting on the pier (due to the sea level rising). Additionally, the overall shapes in the wave trains exhibit the typical feature of nonlinearity after perturbing from its rest state.

2.6. An internal generator

In our present study, the source function f in Eq. (5) is incorporated into the continuity and momentum equations as one type of a net driving force that creates an adverse current, as opposed to our previous study [34]. In this sense, it can be thought of as an internal generator. Given the adverse current speed U_c, the function f is formulated as follows, based on amount of mass flux over the finite volume region specified. This yields

$$f = \frac{(d+\eta)b|U_c^*|}{l_x l_y l_z}\cos\beta = \frac{(d+\eta)|U_c^*|}{l_x l_z}\cos\beta, \tag{50}$$

where (d,b) are the constant water depth and a finite width of the tank, respectively, (l_x, l_y, l_z) represent the size of the rectangular source region in the corresponding coordinates (x,y,z) and β is the same as that of Eq. (47).

Note that $l_y = b$ in Eq. (50), which is one case equivalent to the uniform shape specified in the lateral direction. It is clear that this approximation is straightforward in 2D. In addition, the source strength involves the effects of the surface elevation η at a certain location. By comparison, we found that computations look much more efficient, when the source region covers several cells rather than one cell on a Cartesian grid (see Fig. 13). By rule of thumb, its length (l_x) should be thin (two to three cells) or less than 6% of the wavelength, while the height (l_z) is restricted to distance: from the wave trough below to water depth $(d/3)$ above. To suppress noise from suddenly starting at $t = 0$, the modified speed U_c^* is given by

$$U_c^* = 0.5U_c\{1 + \tanh(10\pi t - \pi)\}, \tag{51}$$

in which $\tanh(t)$ is smoothly varied from -1 to 1 over a specified number of wave periods.

Now, let us observe the effects of the prescribed net driving force: the water surface above the source region (located at $x = 7.89$ to 8.04 m, covering three cells in this case) responds rapidly (ranging from $t = 0.1$ to 0.4 s) and arises to a certain height (see Fig. 6). Closed to the source region, an adverse current generated flows towards two the ends of the tank, forming spatially-varying current profiles in regions of interest, because the current is strongly coupled with incident waves. Interestingly, the mechanism of current generation is through the rapid growth of sea level, similar to the water wave generation by underwater explosion, as gravity is only the restoring force.

2.7. A wave absorber

In the course of modelling of wave propagation, the numerical solution is probably highly sensitive to waves reflected from artificial boundaries, as waves propagate over distance much longer than several wavelengths. To minimize spurious reflection in computations, a less efficient method is to extend the computational domain until a large distance, in which some results are achieved, before the significant reflection error propagates upstream. Additionally, well-suited boundary conditions have to be specified at open boundaries in order to minimize the computer resources required for modelling of an open system. Because no exact absorbing conditions are available at open boundaries, two basic categories recommended are numerical and physical techniques, respectively. In the following, we emphasize how to specify suitable absorbing conditions at the outflow boundary for the confined tank (see Fig. 1), as in this case a well-designed open boundary condition is essential for the semi-open NWT (for example, to effectively reduce the size of the computational domain in length).

2.7.1. Numerical techniques

Two classes of the absorbing boundary conditions are usually applied for handling artificial boundaries. One is based on the wave equation [10] or its zeroth approximation like the open condition [42], where only the waves (asymptotically ideal for low frequencies) leaving the outlet boundary are described. The other relies on the sponge layer or artificial damping zone technique (applicable to absorption of short waves), by means of the addition of a forcing term, and as a result of reduction of oscillations in the solution near the boundary [24]. Mathematically, it is substantially served as a function of the numerical dissipation, by incorporating the appropriate artificial damping terms

$$\vec{F}_\mathrm{d} = (F_\mathrm{d}^x, F_\mathrm{d}^y, F_\mathrm{d}^z) = \{0, 0, -S(x,t)\}\{u, v, w\}^\mathrm{T} \tag{52}$$

implying that only the vertical velocity is modified within the damping zone, corresponding to $S(x) \neq 0$ (see Fig. 7). Owing to definition of one body force, this term ($\vec{F}_\mathrm{d}$) is added to the right-hand side of the NS equations (see Eq. (5) for creating the negative contribution against incident waves. According to the slightly different formulation adopted in [47], the fringe function S defined is given by

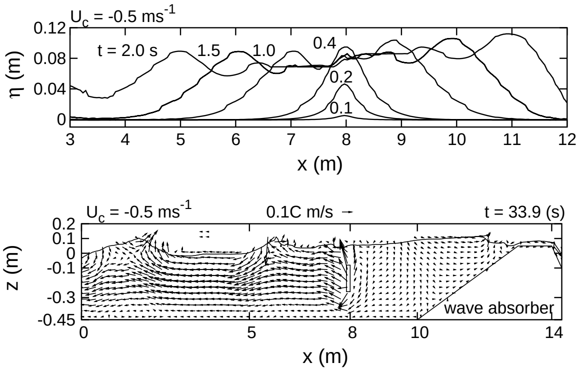

Fig. 6. Spatial variation of tidal elevation from starting initially and the instantaneous velocity fields over grids (291 × 56) for Case 3 (regular waves), by using the internal source function.

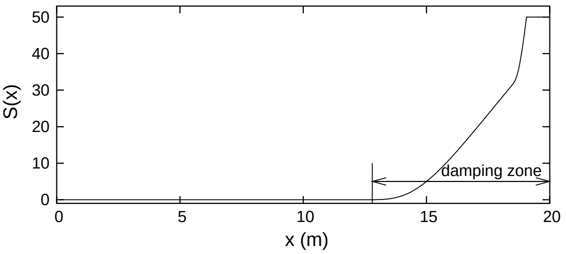

Fig. 7. The damping zone described by the fringe function $S(x)$ for Case 3.

$$S(x,t) = S_{\max}(t)\left\{F\left(\frac{x-x_{\mathrm{s}}}{L\Delta_{\mathrm{rise}}}\right) + F\left(\frac{x-x_{\mathrm{t}}}{L\Delta_{\mathrm{fall}}}+1\right)\right\} \tag{53}$$

with the aid of the length (L) of the computational domain and two coefficients ($\Delta_{\mathrm{rise}}, \Delta_{\mathrm{fall}}$), where $S_{\max}(t)$ is the maximum strength of the fringe function and the subscripts (s, t) stand for the position of two ends (starting and terminal) in the damping zone, respectively. To avoid partial reflection, $S(x)$ is smoothly varied along the damping zone, especially near the entering point. For this reason, $F(r)$ is assigned by

$$F(r) = \begin{cases} 0 & r \leqslant 0, \\ \frac{1}{1+e^{\left(\frac{1}{r-1}+\frac{1}{r}\right)}} & 0 < \mathrm{r} < 1, \\ 1 & r \geqslant 1, \end{cases} \tag{54}$$

as shown in Fig. 7, where the curve plotted in the damping zone (total length of about 1.3λ) consists of three parts, starting from $x = 12.8$ (m) to final step constant value $S_{\max} = 50.0\ \mathrm{s}^{-1}$ near the end wall ($\Delta_{\mathrm{rise}} = 0.6$ and $\Delta_{\mathrm{fall}} = 0.1$ in this case).

In fact, one often couples the sponge layer technique with a piston-like Neumann condition as the hybrid algorithm, which is very efficient in a broader spectrum of waves [6]. Only requirement is to extend the extra length (normally several wavelengths) at the end of a tank so that energy of outgoing waves is effectively dissipated. Consequently, the performance depends heavily on the ratio of the beach length to wavelength λ [5]. Note that such restriction also holds for an internal wavemaker [35], by adding a length at both ends of the tank in general.

2.7.2. A breaking-type wave absorber

We attempt to apply a simple wave absorber, i.e. an artificial sloping ridge is equipped in the extremity of the NWT. It can be considered as one type of physical techniques related with the physical model (see [26] with a perforated metal sheet or [12] for a similar device). In our study, the smooth impermeable structure with constant slope (1/6 or less) is connected to a region with constant water depth, while the top of the structure lies just slightly above the still water level (see Fig. 9, for example). One possible explanation is that the wave energy can be effectively dissipated by breakwaters without the need of adding an extra length, before waves reach its extremity. Accordingly, a simple local boundary condition at the outflow boundary can yield a well-posed solution, especially the wave reflection can be restricted to the minimal level.

A typical example, Case 3 (see Table 1), is selected for testing the performance of a breaking-type wave absorber in 2*D*. By visualizing the typical velocity fields (see Figs. 14–16), the high speed flows are created, while an expanding jet overflows along the crest of the absorber, leading to localized high turbulence. Consequently, dissipation of energy due to waves breaking is the dominant process in the proximity of this absorber, and as a result of a loss of wave energy in breaking waves. For this situation, the reflected waves are expected to be small, which can be convinced in Fig. 8: the general trend of the wave profiles (averaged over 10 periods) and the mean velocity profiles (by interpolation at $x = 7.8$ m) follows closely that of experiments. It reveals that considerable turbulence is rapidly damped out, under the dynamic SGS model. For this reason, our NWT can be made small, which helps to reduce the CPU time.

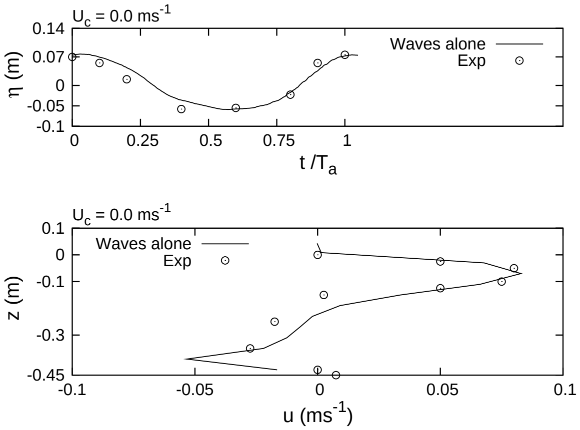

Fig. 8. Comparison between computations and measurements on grids (291 × 56) for Case 3 (regular waves alone): the mean surface elevation and the vertical profiles of mean horizontal velocity, by using the breaking-type wave absorber.

Based on our analysis, the high computational efficiency is achieved, by using a breaking-type wave absorber. This speculation can be further confirmed, by comparison of two types of traditional approaches applied at the outflow boundary: a homogeneous Neumann boundary and the open condition (see Eq. (37). Definitely, such comparison is still of considerable interest for nonlinear water-wave propagation problems, especially when fully turbulent flows are caused by waves breaking.

2.7.3. Comparison of two classes of wave absorbers

As expected, a more interesting reference case is concerned with the homogeneous Neumann boundary (i.e. $\frac{\partial w}{\partial x} = 0$ and $u = 0$, implying a free-slip rigid wall), since there exists a perfect reflecting wall artificially placed at the outlet, where the return flow (undertow) occurs. In contrast of the Neumann boundary, the weakly reflecting condition (see Eq. (37) allows radiating long waves passing through the outlet. Owing to possible generation of the fully (or partially) reflected waves from the boundary, a long domain is useful for both approaches, which should cover a damping zone. Fig. 9 displays reflection and absorption efficiency in terms of the wave train, instantaneous velocity fields and velocity profiles (throughout this paper, the symbol C in the velocity fields drawn stands for the linear shallow wave celerity, unless otherwise stated), when compared with measurements available.

By observation, the perturbations caused by the wall in the early stages are negligible almost everywhere. Probably, there is no serious problem with the simple treatment at the outlet, when modeling of a solitary wave or dam-break flow [23]. After that, the degree of wave reflection varies with the Neumann boundary to breaking-type wave absorber, being strong for the former and practically negligible or weak for the latter (see Fig. 9). This is one example that has been turned out to be very efficient for wave absorption, by using the breaking-type wave absorber (also see Fig. 8). The wave trains, for instance, exhibit typically nonlinear features: high crests and smaller troughs. The fair agreement between predicted and measured results gives partial confirmation: the perfect energy dissipation on a beach with a shorter scale, implying only mildly reflecting.

With the Neumann boundary condition, however, the results are contaminated due to occurrence of appreciable and successive wave reflection, leading to badly-behaved solution. One reason for that is because the incident waves propagate against the return flow to occur under troughs or interact with the reflected waves from the vertical wall or both. Additionally, introduction of the artificial damping zone cannot effectively dissipate the energy of outgoing waves, although the waves progressively lose some energy in this area (see Fig. 9, where the damping zone starts from $x = 16.0$ m). Probably, the waves may be entirely absorbed but less efficient, provided that the length of damping zone is sufficient (the several wavelength or more). The same consequence also holds with the open condition, as in this case an impulsive velocity is generated at the outflow boundary, resulting in the artificially reflected waves there. Consequently, high absorption efficiency of our physical absorbing device and its cost are highlighted by comparison with the two reference simulations men-

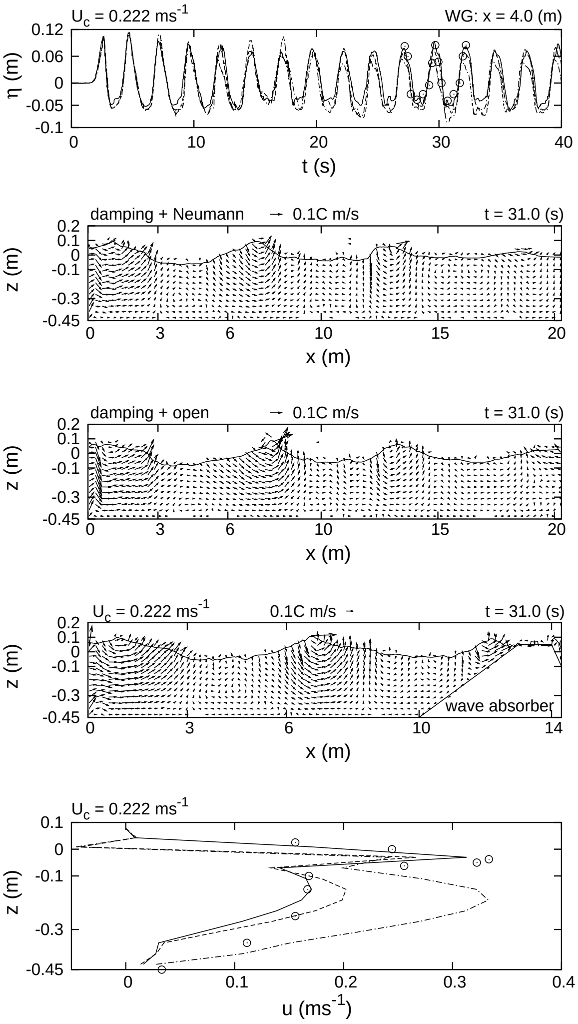

Fig. 9. Comparison of three types of wave absorbers over grids (291 × 56) for Case 3 (the regular following waves): the wave trains at one certain position, subsequent velocity fields and vertical profiles of horizontal velocity (by interpolation at $x = 2.9$ m). —— the breaking-type wave absorber; – – – a Neumann condition plus the damping zone; – · – the open condition plus the damping zone; ⊚ measurements.

tioned. An additional benefit is that it can apply to various wave conditions without the requirement in knowledge of incident waves, except for extra cost adding one simple geometry (a 2D mountain ridge) to our solver.

3. Test cases

To validate the accuracy of our design wave–current generators, five test cases (see Table 1) under consideration are applied, which involve three types of different applications of interest:

- the fully coupled wave–current motions in the open channel over constant water depth (labelled Case 1 to Case 3), for which measurements are available [26,27,12];
- overtopping of violent waves over a vertical barrier, responsible for impact of waves onto the structure, leading to strong reflection at a seawall (referred to as Case 4);
- and overtopping of waves over a seadike, characterized by various physical phenomena in water of varying depth (named Case 5).

When simulating waves following or opposing a turbulent current (Case 1 to Case 3), various theory models are applied and there has been significant progress in this area. Based on the linear wave approximation, for example, Huang and Mei [22] proposed an analytical boundary-layer method for Case 1 plus a little in Case 2. For the latter, more detailed study was achieved by Groeneweg and Battjes [21], according to the generalized Lagrangian mean formulation. Both also involve computations of waves on a negative current, while Fredsøe et al. [12] borrowed the Reynolds-averaged Navier–Stokes (RANS) equations with a k–ω model for solution of the near-bottom motions in Case 3. But the limited values are given in the turbulent regions near the free surface (such as the instantaneous velocity fields), especially the lack of the wave train (importantly, as such assessment helps to observe whether mass conservation holds for a large number of wave periods). Additionally, no one attempts to address grid resolution, which is essential on uncertainty analysis, including the study of convergence issues.

In our present study, all five test cases are demonstrated with our own solver. Definitely, this is very valuable in assessing our design wave–current generators. As illustrated below, we first concern the open channel flow and then study waves on beaches. It is shown that our solver captures most of intrinsic features that would arise in the wave–current interaction, especially it provides more detailed quantitative analysis of the velocity fields plus waves. For example, the surface profiles averaged over 10 periods are given (see Fig. 11) and the mean horizontal velocity profiles at a single station are easily obtained by interpolation at $x = 7.0$ m (see Fig. 12). The computations are performed over a cut-cell grid, which are identical to physical conditions in experiments, except at the bed boundary, where the rough bed in experiments is against the

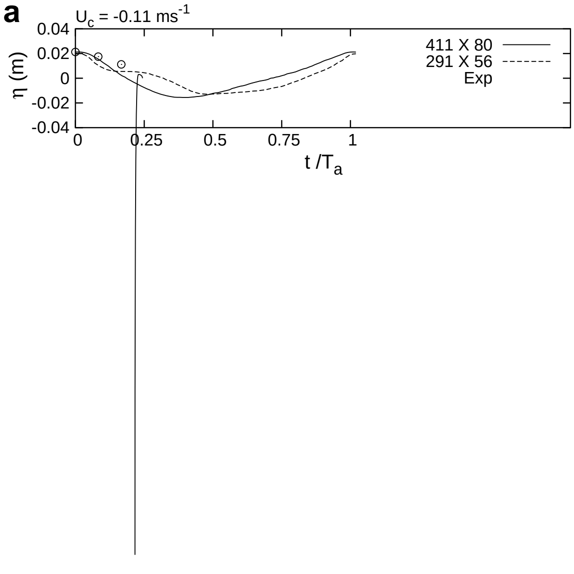

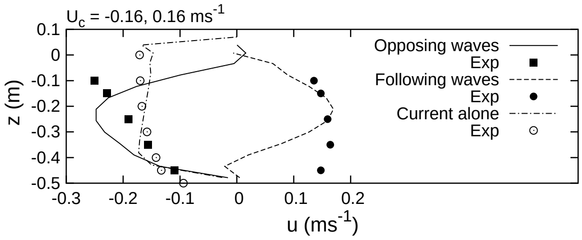

Fig. 12. The vertical profiles of mean velocity under two different currents (positive, negative) over grids (291 × 56) for Case 2 (regular waves), including current-only situation, by using the internal generator.

smooth one in simulations. Two Cartesian grid levels with varying cell sizes are employed for the grid refinement study. The results are represented in terms of the instantaneous velocity fields in 2D (see Fig. 1(b)) and the time history of the surface elevation η (m) at the selected wave gauge (WG), as these variables are directly given, by solving the Navier–Stokes equations with the free surface.

3.1. Wave–current coupling in water of constant depth

As incident waves propagate into the fully developed shear flow, the adverse current is strongly coupled with the waves, forming the opposing waves (see Figs. 14–16). Very encouragingly, our results give the comprehensive comparison for waves on three types of the current states varying with the signed number for Case 1 to Case 3. Definitely, they also provide the physical insight for the interaction of waves with a current. On these figures, a major feature is essentially that waves on an adverse current are shorter than waves on a positive one, as the current compresses the wavelength somehow (see Fig. 10), which is consistent with the point drawn in Eq. (49) for the given values of T_a and d. An expected phenomenon is that the phase-averaged surface profiles display typically nonlinear features, especially in the opposing waves. For the latter, the dynamics of waves can vary significantly with current-induced wave breaking, in case the waves are blocked by the strong opposing currents [7,8], where the change in the gross topology will undergo the processes of merging and breakup. For some particular positive current problems (Case 1 to Case 2), the attenuation of wave heights relative to pure waves is obvious, as the waves are travelling on the current.

Interestingly, the profiles of the longitudinal velocity (u) may fit the sequence near the free surface (see Fig. 12, where the corresponding data are not available in measurements), which display a notable reduction in following waves, as observed in the physical model available (see Fig. 9). According to our computations,

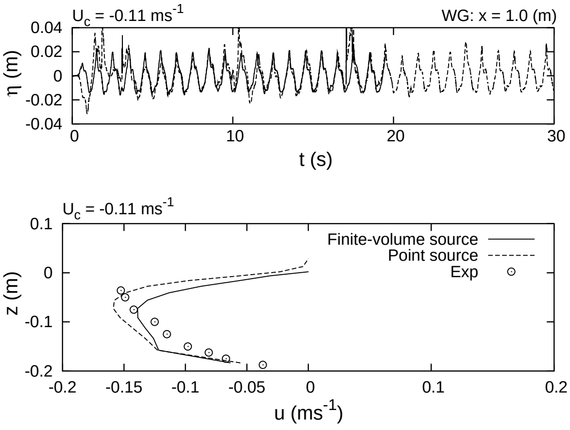

Fig. 13. Comparison of two different source sizes over grids (291 × 56) for Case 1 (the regular opposing waves): the wave train at a certain location and the mean velocity profiles (by interpolation at $x = 1.25$ m), by using the finite-volume source (——) and the point source (– – –), respectively.

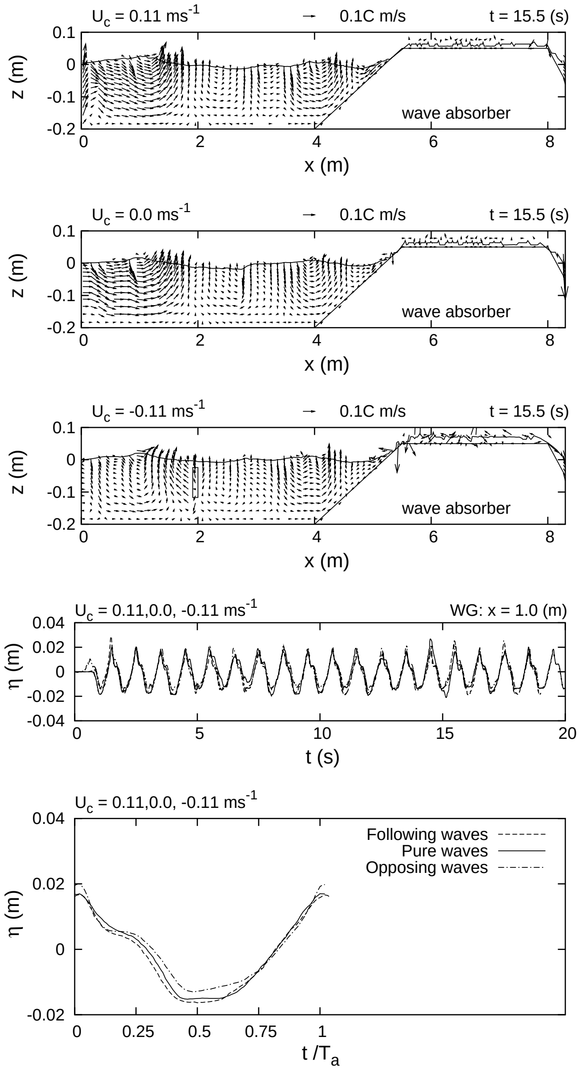

Fig. 14. Following waves, pure waves and opposing waves over grids (291×56) for Case 1 (regular waves): the instantaneous velocity fields, the wave trains at one certain position and the mean surface profiles. – – – $U_c = 0.11$; —— 0.0; – · – -0.11 ms^{-1}.

the predicted velocity diminishes continuously to zero towards two ends of the curve, whether or not there exists a current (also see Fig. 8). One possible explanation is the presence of a transition zone, due to the effects of the surface boundary layer both at the seabed and free surface. For situations where the velocity profiles are predicted well, for example, in the case of following waves, simulation of the wave height tends to be high accurate (see Fig. 11): the shape of the wave profiles may be resolved adequately, especially an excellent agreement between theory and experiment is achieved with increased mesh refinements. In this sense, the discrepancy attributed to the grid effects is relatively small for variable of the wave height (in regular waves). This behavior also holds in the case of the opposing waves but for the velocity profiles the discrepancy is apparent in the proximity of the free surface, where the waves experience an increase in speed towards the free surface (also see Fig. 13). The reason for that is probably attributed the turbulent structures in this area, where the turbulent properties are highly anisotropic [49]. On the other hand, the wave boundary layer is likely to extend up into the current-induced logarithmic layer. A local adaptive mesh adjacent to interfaces is attractive for capture of the fully developed turbulent boundary layer. In the near-bottom region, the different local features are partly due to different seabed conditions regardless of resolution that is employed.

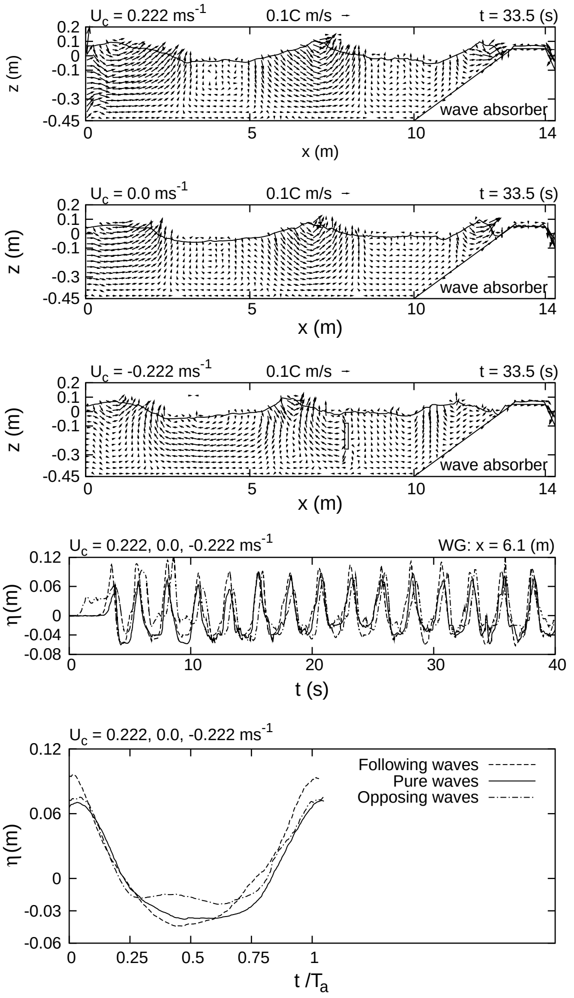

Fig. 16. Following waves, pure waves and opposing waves over grids (291 × 56) for Case 3 (regular waves): the instantaneous velocity fields, the wave trains at a certain location and the mean surface profiles. – – – $U_c = 0.222$; —— 0.0; – · – -0.222 ms^{-1}.

By visualizing the wave-induced motions in regions of interest with several stages (see Fig. 18), it is found that flows become highly turbulent under waves breaking, often subjected to identifiable jet-splash cycles, when waves overtop over the seadike. After that, the breaking waves transform into a turbulent bore, characterized by a steep turbulence front and an area of recirculating flow. In the wave front, the particle velocity exceeds the speed limit underneath the region of flows, leading to the rapid increase in high turbulent kinetic energy ($t = 32.4$ s, for example). Interestingly, there exists two possible sources of turbulence generation for waves on beaches. One is the initial instability that leads to breaking, because of continuous increase of the wave steepness ($t = 4.5$ s); the other is the proceeding of the downwash, which also induces waves breaking ($t = 33.4$ s). Definitely, the presence of a current modifies wave characteristics, especially in regions subjected to strong turbulent flows, where a large hydraulic jump is created nearby at $x = 4.0$ m ($t = 32.2$ s), under certain circumstance of irregular waves alone.

In contrast to this, the positive current stretches the wavelength, leading to reduction in the steepness of waves. Consequently, the wave–current interaction tends to be less severe, probably similar to computations in deep water waves, characterized by a thick sheet of water on the beach (defined as the so-called swash), in which the nonlinearity is weak. Such effects tend to be considerable in general, as a current increases.

On the other hand, the wave pattern develops rapidly after the transient phase and highly sharp-crest waves (i.e. one typical feature of irregular waves) are well captured (see Fig. 17), which always occur in real sea. As expected, the phase shift is the result of the Doppler effects due to the presence of a current. Interestingly, the high turbulence activity occurs at phase mostly within the surf zone, subjected to rapid deformation of the free surface, where the eddy viscosity ν_t dominates over the molecular viscosity ν (see Fig. 17 for varying with ν_t).

3.3. 3D effects

To observe the 3D effects, the source of the wavemaker in 2D (ranging from the bottom to the free surface) is uniformly distributed along the inlet section extended to the width of 1.0 m. Geometrically, this shape constructs a cubic tank of edge length $6.3 \times 1.0 \times 1.0\ \text{m}^3$ separately in the longitudinal, lateral and vertical directions (see Fig. 1(a)). For the present 3D seadike problem, any longitudinal profile is identical with the 2D case (see Fig. 1(b), referred to as the symmetry plane of $y = 0$, for convenience). Based on the usual CFD validation procedure, the convergence performance is first discussed for regular waves alone, and then computations with different grids are conducted for investigation of the asymptotic grid convergence. Accordingly, an interesting comparison between 3D and 2D cases is described. Finally, the asymmetry of flows at the cross-sections (i.e. the y–z plane) is detected for various horizontal positions in the presence of a current or not. Summarily, our results demonstrate that the gravity-wave breaking is essentially a three-dimensional process only in the surf zone (where the flow shape loses its symmetry and becomes fully 3D), as surface waves move up the slope, resulting in a 3D convective instability. In this sense, the wave propagations differ substantially from strong internal waves that may cause intense shear in 3D [3].

3.3.1. Convergence history

By examining the L_2 norm of the residuals (Res), $\text{Res}_\varphi = \{\sum_{m=1}^{N}(\varphi^n_{i,j,k} - \varphi^{n-1}_{i,j,k})^2/N\}^{\frac{1}{2}}$ with the total number of cells N and $\varphi = (U, V, W, P)$, Fig. 19 exhibits a set of the convergence history in iterations for the momentum equations (U, V, W) in the (x, y, z)-directions plus the pressure (P). In this case, computations are conducted over one single mesh $(205 \times 21 \times 40)$ with varying cell sizes, except in the y-direction, where the grid spacing is uniform.

As expected, the fast convergence rate about the pressure is achieved due to the computationally efficient algorithm developed in our solver. This is divided into two regimes according to the trend of curves: first to decay nearly exponentially with a relatively short time and then turns to the flat until a certain time level specified by a user (see Fig. 19). Based on the fact that solution of the pressure-Poisson equation is essentially the most time-consuming part for any incompressible flow problems, therefore, our solve exhibits the well overall performance in computations. Furthermore, mass conservation ensures that our simulations are stable even during lengthy computations. This is because errors are eliminated exponentially with the iterative number, in case the errors in mass are mainly caused by the residuals from the continuity equation (in fact, these are principally composed of high-frequency error components [36]). According to a decoupled approach, it

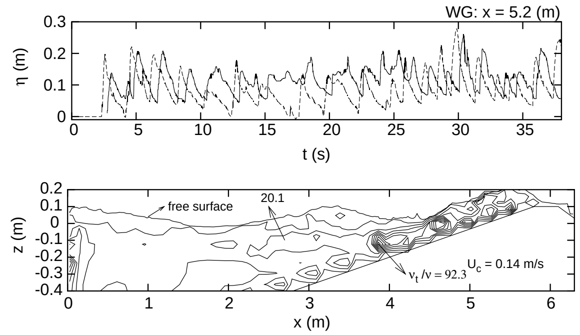

Fig. 17. Current effects over grids (251×40) for Case 5 (irregular waves): the time history of the surface elevation at one wave gauge selected and the eddy viscosity contours (ν_t/ν) at $t = 32.2$ s (magnified view: 5 to 100 with interval 10). —— $U_c = 0.14\ \text{ms}^{-1}$; – – – $U_c = 0.0$.

available is achieve

inlet), as a mesh inc

schemes to dissipat

fields (see Fig. 21),

Such coherent turb

enon causes asymn

(defined by $\omega_x = \frac{\partial w}{\partial y}$

identical with the c

3.3.3. Comparison

On the assumpti

observation for this

similar to those in 2

tion adjacent to the

evidence: waves in

solver coupled with

configuration in 2D

as compared to 2D

sient from rest. Of c

the generation of h

profiles.

Before breaking,

simulations are alm

ary circulation usua

with a strong centr

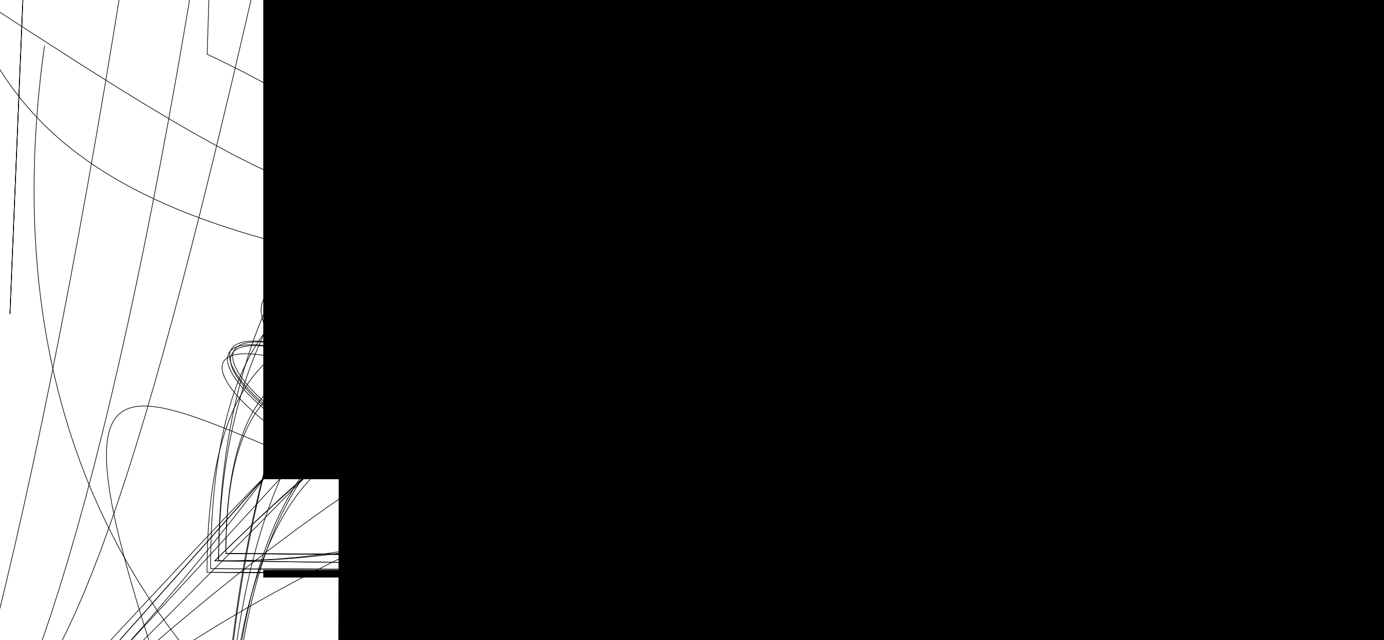

Fig. 22. Comparison of 3D with

—— 3D (205 × 21 × 40); – – – 2

predicted secondary current is rather weak, based on the results in 2D and 3D at the same position (see Fig. 22: $x = 2.02$ m), indicating that small disturbances in 3D are not sufficient to affect the two-dimensional results (although the results in 3D look better). This is consistent with the study in [21], as the secondary circulations tend to be one or two orders of magnitude smaller than the longitudinal velocity.

Owing to stretch and intensification in shear, the three-dimensional dynamic characteristic of the motions will grow up rapidly in the surf zone during waves breaking, and as a result of an initial two-dimensional con-

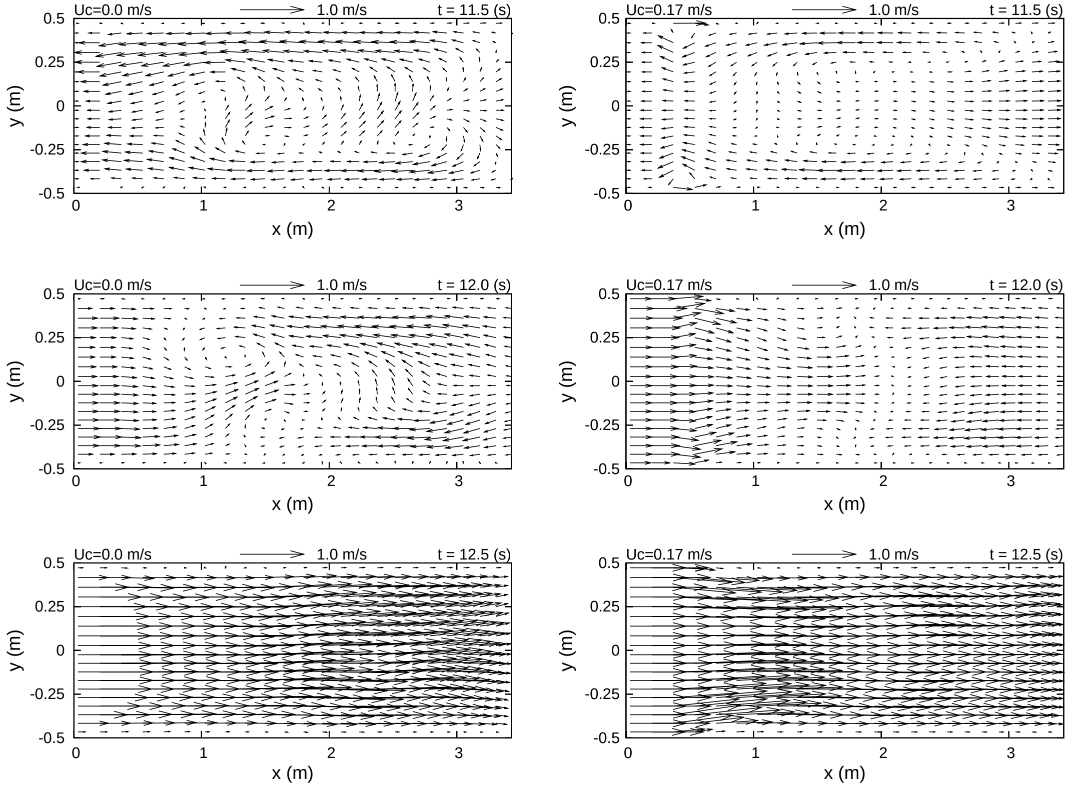

Fig. 24. Sidewall effects on the longitudinal motions in 3D over grids ($205 \times 21 \times 40$) for Case 5 (regular waves): the instantaneous velocity fields varying with three time levels (a fixed vertical position of $z = -0.28$ m).

there is no obvious sign for the strong coupling between the transverse and longitudinal dynamics, due to the weak solution of the lateral motions (see Fig. 23). Consequently, the effect of the longitudinal scale on the horizontal velocity is dominant over that of the cross-sectional part. As a highly turbulent bore generated propagates along the beach, the obliquely descending eddies, found by Nadaoka et al. [41] in experiments, can also be described by the velocity vectors in the plane (see Fig. 24: $t = 12.0$ s). Such turbulent structures in 3D behave a pair of counter-rotating vortices, forming the three-dimensional vorticity fields but decay with time or destroy. Interestingly, the influence of walls may not be only the three-dimensional forcing from which the instability develops [19], as for waves on beaches high turbulence in 3D can be induced by the breaking waves.

Physically, the near-wall motions are substantially suppressed by the sidewall boundary-layer thickness, while varying with the addition of even the small current (see Fig. 24). Sufficiently far from the walls (perfectly in the center of plane, $y = 0$), the significant influence of the sidewall does not detected. Anyway, this effects could be further reduced by use of a wider flume, especially the width of a tank becomes infinite. Note that the flows become three-dimensional (although weak) at toe of the dike (see Fig. 23: $x = 1.0$ m), due to the longitudinal modulation of the bottom topography. In fact, only within the breaking region, the motions are significantly three-dimensional (see Fig. 23: $x = 4.5$ m), where the surface profile shows pronounced local lateral variability, and as a result of advection of a larger-scale three-dimensional feature from the swash zone.

4. Conclusions

By design of the different wave–current generators applied to the NWT, we study interactions of breaking waves with currents over a structure, based on a dynamic Smagorinsky model. Computations are conducted on Cartesian cut-cell grids with our developed Navier–Stokes solver. By superimposing a steady current onto waves, our external generator technique provides well-defined wavy inflow conditions, which have been addressed in the study of waves following a current. For waves propagating against strong currents, the internal source function introduced is used as one type of a net driving force for creation of the desirable opposing current, forming our internal generator.

Our solver has be extensively illustrated with five test cases studied. These are of particular values in distinctly different applications, especially in the area of nonlinear shallow water-wave propagation problems, significantly characterized by overtopping of waves. Given finite amplitude surface water waves, we concern a direct comparison of the numerical simulation with the experimental flows varying with different currents (positive, zero, negative). By validation, the results in 2D or 3D agree well with measurements available in terms of the wave or horizontal velocity profiles. Hopefully, our study can provide valuable base for the analysis of wave–current-structure coupling, induced by regular and irregular waves. The major conclusions are drawn as follows:

- The grid dependency is still a crucial aspect for our VOF-based solver. Near the free surface, for example, the minimum grid space (in the vertical direction) varies with case by case. When validated the results, visualization of the wave pattern plus the instantaneous velocity fields are both important, based on our experience.
- By using a breaking-type wave absorber, the reflected waves can be effectively dissipated without loss of the flow characteristics of interest, which differs substantially from various theoretical schemes proposed for absorbing waves reflected at the outflow boundary. In this sense, our computations are without the instability problems even for a long duration. This is very useful for situations involving some actual cases, as the lengthy computations are necessary, especially such information helps to confirm whether the global mass and energy are conserved.
- Under the test for waves against the adverse current, the dynamics of flows could more dramatically vary, as in this case the waves shorten the wavelength, relative to waves superimposed on the positive current. Owing to existence of a transition zone (related with two different roughness values caused by the actual bed and free surface), our results reveal that the flow is increased in the outer layer after a drop in the logarithmic description of the velocity profiles, vanishing at the free surface. This is true for waves following a current but in the situation of opposing waves it appears that growth of the mean horizontal velocity is underestimated, as compared to measurements available.
- Owing to the lack of the spanwise convective rolls, the physical dissipation for the two-dimensional flow is substantially limited in the case of waves breaking. On the other hand, wave dynamics remains two-dimensional in regions of non-breaking waves but the dominant motions in the surf zone are obviously a three-dimensional convective instability that leads to spanwise convective rolls. It is clear that the disturbance caused by 3D enhances the strength of this instability at the expense of waves breaking.

Ongoing and future work will incorporate the particular adverse current case for the study of wave blocking.

Acknowledgments

The present work is supported by the Funds for Scientific Research – Flanders, Belgium (Project No. G.0199.06). Additionally, we also thank the two referees for their helpful suggestions.

Appendix A

A.1. Effects of a dynamic SGS model on MILES in breakwaters

More recently, irrotational flow models are still widely applied for wave–current interactions, in case the effects of viscosity and vorticity are weak, as studied in [8,55] with the Boussinesq-type equations. Under breaking waves, however, the flows become complex unsteady flows. To confront the scale-complexity problem inherent to turbulent flows, the technique of LES has emerged as an alternative to the RANS approach [14]. In the context of this theory, MILES probably provides a promising practical tool due to without any further modelling: it lets the numerical viscosity dampen the numerical simulation, by introducing high-resolution locally monotone algorithms [15]. More specifically, an elementary approach in MILES is to discretize the convective terms, based on the schemes like Jameson, MUSCL and ENO [9,16]. But a hybrid approach (called MILES + SGS in our study), constructed by MILES that is coupled with a dynamic SGS model, is essential for accurate estimation of periodic breaking water-wave propagation problems, especially for the lengthy computations, as the SGS model incorporates a model bringing a turbulent viscosity. The discussion regarding the issues is given as follows.

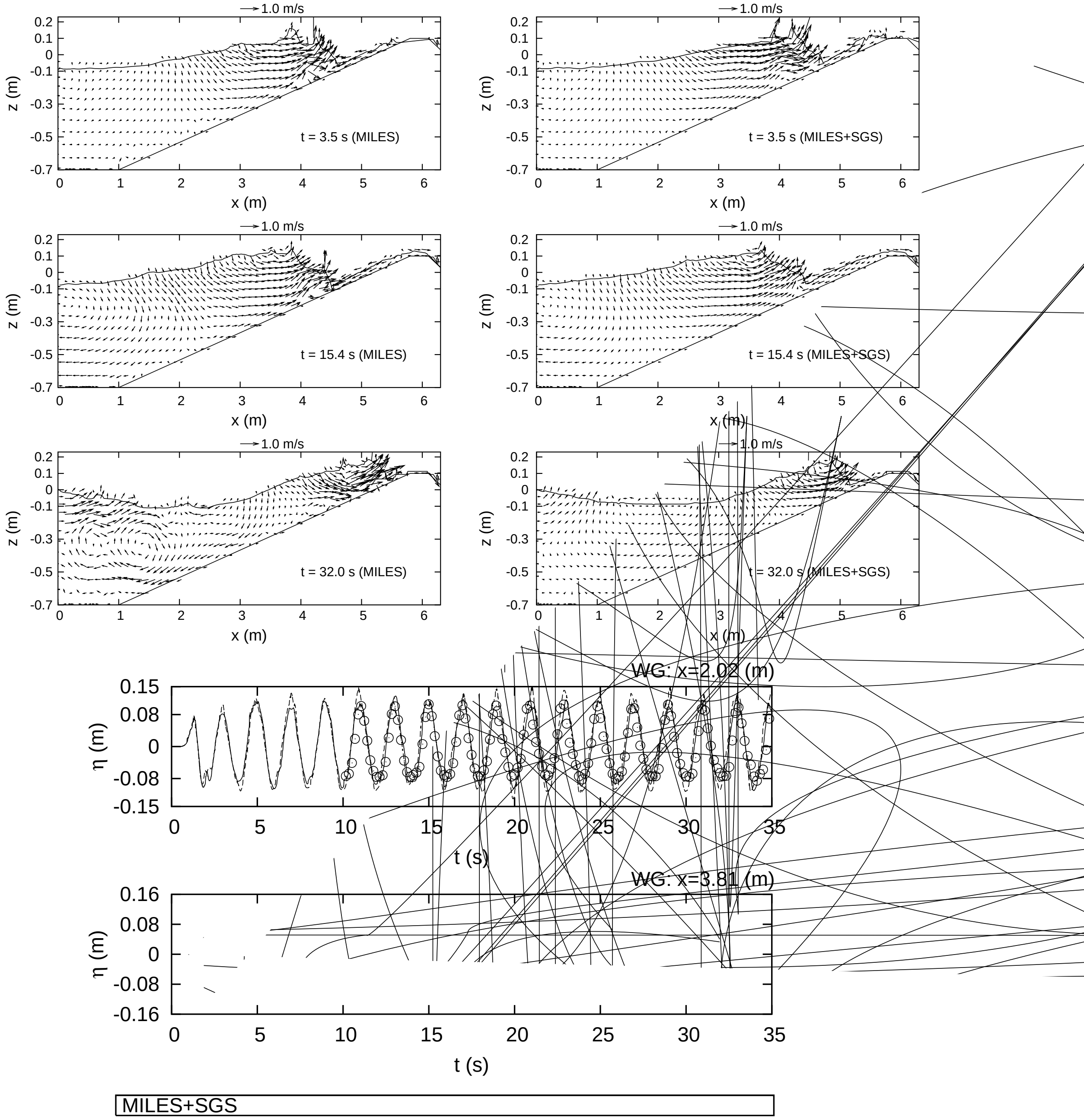

Flows behave as localized high turbulence in waves breaking, as given with two typical case studies related to coastal structures (see Figs. 25 and 26), leading to the rapid increase in high turbulent kinetic energy. But the energy of waves accumulated at the high wavenumbers can be effectively dissipated by turbulence, when using a dynamic SGS model. Otherwise, the spurious currents are probably generated only with MILES, and as a result of the damage to true solution at the same grid. Hopefully, this provides one example: MILES cannot resolve LES properly [46], in case the principal mechanism of turbulence diffusion is through the action of viscous on the breaking waves.

When the flows become self-sustaining turbulence, the wave-induced motions evolve into the following two distinct parts: (i) In the early stage, the viscous effects may be regarded as negligible, and the results look very

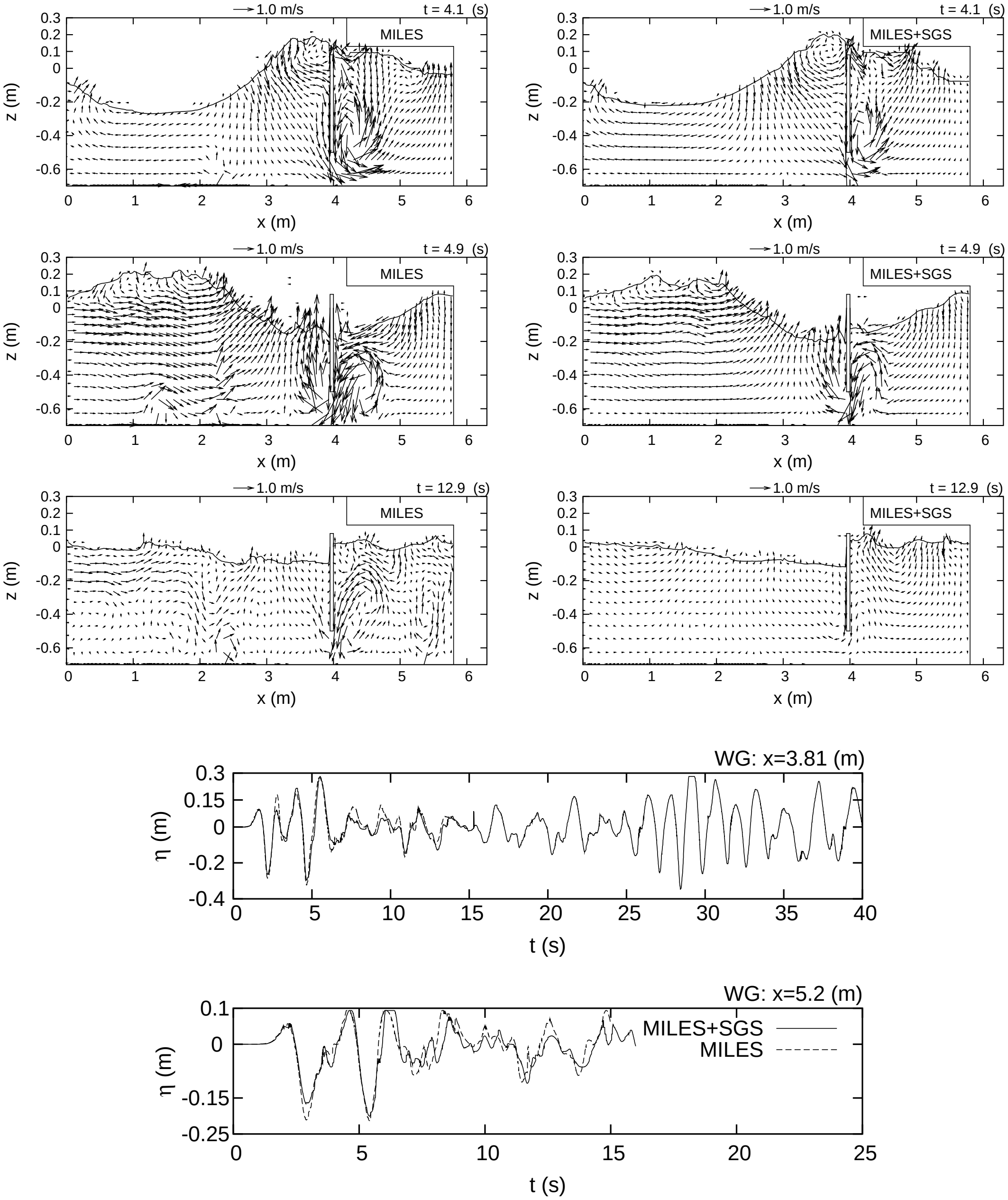

Fig. 26. Comparison between MILES and MILES + SGS over grids (251 × 40) for Case 4 (pure irregular waves): the instantaneous velocity fields and the wave trains at two certain locations.

close except for a small phase shift (also see [30] with our shock-capturing Euler solver), as in this case the leading-order truncation error (growing with increasing wavenumber) acts as the intrinsic SGS model that dissipates the energy of waves. It means that our MILES approaches capture well growth rates of the initial perturbation, caused in waves breaking. Consequently, the total contribution of the turbulence increase can be almost balanced under the numerical dissipation mechanism. (ii) Nevertheless, different features are apparent in waves continuously breaking, and viscous diffusion plays an important role in the flow regime eventually dominated by turbulence. After the initiation of progressive waves breaking, the performance of MILES is far from satisfactory in terms of the surface profiles (as a function of time), especially for the flowfield. A major reason is that the numerical viscosity in MILES cannot restrain the increase of energy fluctuated on a broad range of length and time scales, partly due to insufficient grid resolution or the frequent occurrence of small-scale structures or both. On the contrary, the hybird scheme maintains a transfer of energy in the nearly equilibrium state of turbulence field, by modelling of small-scale turbulent fluctuations, responsible for the kinetic energy dissipation. MILES + SGS is probably a more viable approach for breaking water-wave problems, therefore, based on the fact that SGS models provide an additional physics mechanism, by which dissipation of a rapid build-up of kinetic energy at high wavenumber can occur [16]. This behavior is particularly important in waves breaking.

References

[1] K. Anthony, P. Ugo, B. Elias, A priori and a posteriori tests of inflow conditions for large-eddy simulation, Phys. Fluids 16 (3) (2004) 4696–4712.
[2] J.A. Battjes, Surf-zone dynamics, Ann. Rev. Fluid Mech. 20 (1988) 257–293.
[3] S. Belcher, J. Hunt, Turbulent flows over hills and waves, Ann. Rev. Fluid Mech. 30 (1998) 507–538.
[4] N. Booij, R.C. Ris, L.H. Holthuijsen, A third-generation wave model for coastal regions, Part I, model description and validation, J. Geophys. Res. 104 (C4) (1999) 7649–7666.
[5] M.S. Celebi, M.H. Kim, R.F. Beck, Fully nonlinear 3-D numerical wave tank simulation, J. Ship Res. 42 (1998) 33–45.
[6] A. Clément, Coupling of two absorbing boundary conditions for 2D time-domain simulations of free surface gravity waves, J. Comput. Phys. 126 (1996) 139–151.
[7] A. Chawla, J.T. Kirby, Monochromatic and random wave breaking at blocking points, J. Geophys. Res. 107 (2002) 1–19.
[8] Q. Chen, Per A. Madsen, H.A. Schäffer, D.R. Basco, Wave–current interaction based on an enhanced Boussinesq approach, Coast. Eng. 33 (1998) 11–39.
[9] F.K. Chow, P. Moin, A further study of numerical error in large-eddy-simulation, J. Comput. Phys. 184 (2003) 366–380.
[10] B. Engquist, A. Majda, Absorbing boundary conditions for the numerical simulations of waves, Math. Comput. 31 (1977) 629–651.
[11] J.H. Ferziger, Large eddy simulation, in: M.Y. Hussaini, T. Gatski (Eds.), Simulation and Modelling of Turbulent Flows, Cambridge University Press, New York, 1995.
[12] J. Fredsøe, K.H. Andersen, B.M. Sumer, Wave plus current over a ripple-covered bed, Coast. Eng. 38 (1999) 177–221.
[13] O.B. Fringer, R.L. Street, The dynamics of breaking progressive interfacial waves, J. Fluid Mech. 494 (2003) 319–351.
[14] U. Frisch, Turbulence, Cambridge University Press, Cambridge, UK, 1995.
[15] C. Fureby, F.F. Grinstein, Large eddy simulation of high-Reynolds-number free and wall-bounded flows, J. Comput. Phys. 181 (2002) 68–97.
[16] E. Garnier, M. Mossi, P. Sagaut, P. Comte, M. Deville, On the use of shock-capturing schemes for large-eddy simulation, J. Comput. Phys. 153 (1999) 273–311.
[17] M. Germano, U. Piomelli, P. Moin, W. Cabot, A dynamic subgrid-scale eddy viscosity model, Phys. Fluids 3 (1991) 180–200.
[18] S. Ghosal, T.S. Lund, P. Moin, K. Akselvoll, A dynamic localization model for large-eddy simulation of turbulent flows, J. Fluid Mech. 286 (1995) 229–255.
[19] F. Gheusi, J. Stein, O.S. Eiff, A numerical study of three-dimensional orographic gravity-wave breaking observed in hydraulic tank, J. Fluid Mech. 410 (2000) 67–99.
[20] W.D. Grant, O.S. Madsen, Combined wave and currents interaction with a rough bottom, J. Geophys. Res. 84 (1979) 1797–1808.
[21] J. Groeneweg, J.A. Battjes, Three-dimensional wave effects on a steady current, J. Fluid Mech. 478 (2003) 325–343.
[22] Z. Huang, C.C. Mei, Effects of surface waves on a turbulent current over a smooth or rough seabed, J. Fluid Mech. 497 (2003) 253–287.
[23] K.M.T. Kleefsman, G. Fekken, A.E.P. Veldman, B. Iwanowski, B. Buchner, A volume-of-fluid based simulation method for wave impact problem, J. Comput. Phys. 206 (2005) 363–393.
[24] M. Israeli, S.A. Orszag, Approximation of radiation boundary condition, J. Comput. Phys. 41 (1981) 115–135.
[25] F.J. Kelecy, R.H. Pletcher, The development of a free surface capturing approach for multidimensional free surface flows in closed containers, J. Comput. Phys. 138 (1997) 939–980.
[26] P.H. Kemp, R.R. Simons, The interaction between waves and a turbulent current: waves propagating with the current, J. Fluid Mech. 116 (1982) 227–250.

[27] G. Klopman, Secondary circulation of the flow due to waves and currents: laser-Doppler flow measurements for waves following or opposing a current, Technical Report Z2249, Delft Hydraulics, 1997.

[28] M. Lesieur, O. Metails, New trends in large eddy simulations of turbulence, Annu. Rev. Fluid Mech. 28 (1996) 1–45.

[29] D.K. Lilly, A proposed modification of the Germano subgrid-scale closure method, Phys. Fluids A 4 (1992) 633–635.

[30] T. Li, P. Troch, J. De Rouck, Wave overtopping over a sea dike, J. Comput. Phys. 198 (2004) 686–726.

[31] T. Li, P. Troch, J. De Rouck, D. Goossens, Numerical simulation of water wave impacts using a Navier–Stokes solver, in: Proceedings of the 29th International Conference on Coastal Engineering, vol. 4, 2004, pp. 4100–4112.

[32] T. Li, Computation of turbulent free-surface flows around modern ships, Int. J. Numer. Meth. Fluids 43 (2003) 407–430.

[33] T. Li, A LVOF user guide, Technical Report, Department of Civil Engineering, Ghent University, Belgium, 2006.

[34] T. Li, P. Troch, J. De Rouck, On the study of wave–current-structure interactions in a numerical wave tank, in: Proceedings of the 16th International Offshore and Polar Engineering Conference, vol. 3. 2006. pp. 356–362.

[35] P. Lin, P.L.F. Liu, Internal wave-maker for Navier–Stokes equations models, J. Waterway Port Coast Ocean Eng. 4 (1999) 207–215.

[36] D. Lörstad, L. Fuchs, High-order surface tension VOF-model for 3D bubble flows with high density ratio, J. Comput. Phys. 200 (2004) 153–176.

[37] M.S. Longuet-Higgins, R.W. Stewart, The changes of amplitude of short gravity waves on steady non-uniform currents, J. Fluid. Mech. 10 (1961) 529–549.

[38] P. Lubin, S. Vincent, S. Abadie, J.P. Caltagirone, Three-dimensional large eddy simulation of air entrainment under plunging breaking waves, Coast. Eng. 52 (2006) 631–655.

[39] C. Meneveeau, T.S. Lound, W.H. Cabot, 1A Lagrangian dynamic subgrid-scale model of turbulence, J. Fluid Mech. 319 (1996) 353–385.

[40] F.M. Najjar, D.K. Tafti, Study of discrete test filters and finite difference approximations for the dynamic subgrid-scale model, Phys. Fluids 8 (1996) 1076–1088.

[41] K. Nadaoka, M. Hino, Y. Koyano, Structure of the turbulent flow field under breaking waves in the surf zone, J. Fluid Mech. 204 (1989) 359–387.

[42] I. Orlanski, A simple boundary condition for unbounded hyperbolic flows, J. Comput. Phys. 21 (1976) 251–269.

[43] J.C. Park, M.H. Kim, H. Miyata, Three-dimensional numerical wave tank simulations on fully nonlinear wave–current–body interaction, J. Mar. Sci. Technol 6 (2001) 70–82.

[44] D.H. Peregrine, Interaction of water waves and currents, Adv. Appl. Mech. 16 (1976) 9–117.

[45] U. Piomelli, J. Liu, Large-eddy simulation of rotating channel flows using a localized dynamic model, Phys. Fluids 5 (7) (1995) 839–848.

[46] P. Sagaut, Large Eddy Simulation for Incompressible Flows, third ed., Springer, 2005.

[47] P. Schlatter, N.A. Adams, L. Kleiser, A windowing method for periodic inflow/outflow boundary treatment of non-periodic flows, J. Comput. Phys. 206 (2005) 505–535.

[48] J.U. Schlüter, H. Pitsch, P. Moin, Large eddy simulation inflow conditions for coupling with Reynolds-averaged flow solvers, AIAA 42 (3) (2004) 478–484.

[49] L. Shen, D.K.P. Yue, Large-eddy simulation of free-surface turbulence, J. Fluid Mech. 440 (2001) 75–116.

[50] J. Smagorinsky, General circulation experiments with the primitive equations, Part I: the basic experiment, Mon. Weather Rev. 91 (1962) 99–152.

[51] O.V. Vasilyev, T.S. Lund, P. Moin, A general class commutative filter for LES in complex geometries, J. Comput. Phys. 146 (1998) 82–104.

[52] B. Vreman, B. Geurts, H. Kuerten, On the formulation of the dynamic mixed subgrid-scale model, Phys. Fluids 6 (12) (1994) 4057–4059.

[53] Y. Watanabe, H. Saeki, Three-dimensional large eddy simulation of breaking waves, Coast. Eng. 41 (1999) 281–301.

[55] S.B. Yoon, P.L.F. Liu, Interaction of currents and weakly nonlinear water waves in shallow water, J. Fluid Mech. 205 (1989) 397–419.